DOT/FAA/TC-13/8

Federal Aviation Administration
William J. Hughes Technical Center
Aviation Research Division
Atlantic City International Airport
New Jersey 08405

Feasibility of Anti-Icing Airfield Pavements Using Conductive Concrete and Renewable Solar Energy

April 2013

Final Report

This document is available to the U.S. public through the National Technical Information Services (NTIS), Springfield, Virginia 22161.

This document is also available from the Federal Aviation Administration William J. Hughes Technical Center at actlibrary.tc.faa.gov.

U.S. Department of Transportation
Federal Aviation Administration

NOTICE

Technical Report Documentation Page

1. Report No.	2. Government Accession No.	3. Recipient's Catalog No.
DOT/FAA/TC-13/8		

4. Title and Subtitle	5. Report Date
FEASIBILITY OF ANTI-ICING AIRFIELD PAVEMENTS USING CONDUCTIVE CONCRETE AND RENEWABLE SOLAR ENERGY	April 2013
	6. Performing Organization Code

7. Author(s)	8. Performing Organization Report No.
Ernie Heymsfield, Adam B. Osweiler, R. Panneer Selvam, and Mark Kuss	

9. Performing Organization Name and Address	10. Work Unit No. (TRAIS)
University of Arkansas Fayetteville, AR 72701	
	11. Contract or Grant No. Grant No.10-G-011

12. Sponsoring Agency Name and Address	13. Type of Report and Period Covered
Federal Aviation Administration Airport Engineering Division (AAS-100) 800 Independence Avenue SW Washington, DC 20591	Final Report
	14. Sponsoring Agency Code AAS-100

15. Supplementary Notes

The Federal Aviation Administration Aviation Research Division COR was Donald Barbagallo.

16. Abstract

Snow, ice, and slush pavement conditions significantly impact aircraft landing, takeoff, and ground operational safety. Snow removal operations, involving plowing and chemical treatment, are costly to airport operators and result in delays to the traveling public. This report presents an alternative approach that combines photovoltaic energy with conductive concrete to develop an anti-icing airfield pavement to prevent snow/ice accumulation. This approach maintains the concrete slab surface at an above-freezing temperature using direct current energy supplied by a photovoltaic and battery system. To test this approach, the University of Arkansas Engineering Research Center constructed a series of conductive concrete overlay test sections. The thermal mass properties of concrete were used in this work to minimize energy demands. Energy was continually supplied to the concrete mass to maintain a uniform temperature and, therefore, to negate the need of an energy surge to remove snow.

Although the conductive concrete test sections showed some heat gain from the photovoltaic energy system, the overall heat gain was not sufficient to ensure reliable snow-melting capabilities during cold and windy conditions. Additionally, the costs for additional photovoltaic cells and batteries necessary to supply the energy needed for the system would result in poor cost-to-benefit ratios.

17. Key Words	18. Distribution Statement
Anti-icing, Renewable energy, Pavement, Conductive concrete	This document is available to the U.S. public through the National Technical Information Service (NTIS), Springfield, Virginia 22161. This document is also available from the Federal Aviation Administration William J. Hughes Technical Center at actlibrary.tc.faa.gov

19. Security Classif. (of this report)	20. Security Classif. (of this page)	21. No. of Pages	22. Price
Unclassified	Unclassified	65	

ACKNOWLEDGEMENTS

The authors are appreciative of the Federal Aviation Administration's financial support of this research work. The authors thank Donald Barbagallo, Joseph Breen, and Ryan King of the Federation Aviation Administration for their guidance during this project. The authors also acknowledge the guidance and material sample contributions by Albert Tamashausky of Asbury Graphite Mills, Inc. The contents of this report reflect the views and opinions of the authors and do not necessarily reflect the views of the Federal Aviation Administration.

TABLE OF CONTENTS

LIST OF FIGURES

LIST OF TABLES

LIST OF SYMBOLS AND ACRONYMS

$\frac{\partial Q}{\partial t}$	Heat generation rate per unit volume
ρ	Average electrical resistivity of a material (p. 12) mass density (p. 43)
Ω-in.	Ohm-inch, or inches ohm, a measure of electric resistivity
A	Cross-sectional area of the testing material parallel to the electrodes through which the current flows
C_p	Material-specific heat
$f'c$	*Concrete compressive strength*
h_B	Convective heat transfer coefficient
I	Known current
κ	Electrical conductivity
k	Thermal conductivity
L	Electrode spacing
n_α	Normals
q_n	Heat flux normal to the boundary surface
q_{cvB}	Convection heat flux at the boundary
R	Resistance
T	Temperature
t	Time
V	Voltage, or electrical potential
AC	Alternating current
BFS	Blast furnace slag
DAQ	Data acquisition
DC	Direct current
FAST	Fixed automatic spray technology
HRWR	High-range water reducer
MSP	Minneapolis-St. Paul International Airport
PV	Photovoltaic
UA	University of Arkansas
w/c	Water/cement ratio

EXECUTIVE SUMMARY

Snow, ice, and slushy pavement conditions significantly impact aircraft landing, takeoff, and operational safety. Current snow removal efforts can be costly and labor-intensive for airport operators to effectively maintain pavement safety during winter conditions. Additionally, inclement cold weather conditions significantly impact aircraft scheduling. This report presents an alternative approach for snow removal in which photovoltaic, or solar, energy is coupled with conductive concrete to develop an anti-icing airfield pavement. By maintaining the pavement slab surface at an above-freezing temperature, snow and ice accumulation are prevented.

An anti-ice concrete slab was developed in this study by supplying direct current energy from a photovoltaic energy system to a conductive concrete pavement overlay. During this study, the University of Arkansas (UA) Engineering Research Center constructed a 20- by 24-ft test mat to substantiate the methodology. The test mat consisted of ten 4- by 10-ft conductive concrete overlay panels and two 4- by 10-ft control concrete overlay panels. The two control panels made of conventional concrete were used as a basis for the conductive concrete overlay panel results. A conductive concrete mix was specially formulated for this study. This report documents the test results.

Unfortunately, due to mild winter weather trends, the system was not tested under winter snow conditions. Instead, experiments were conducted by supplying energy to test panels and then recording surface temperature changes. Panels were also energized using stored battery energy and a layer of ice was applied to the mat surface to simulate icy conditions. Although the panels showed good results, they required more energy than would be economical.

The study identified several difficulties in developing a system that incorporates solar energy and conductive concrete overlay panels to create an anti-icing slab. For example, in a Nebraska heated bridge deck system, 4-in. conductive concrete overlay panels were used; however, energy for that project was supplied through a high-voltage energy grid. Conversely, in the system described in this report, energy was supplied through renewable solar energy in which voltage and amperage are constrained due availability and cost. Findings from this study suggest that the 4-in. thickness of the overlay panel needs to be reduced and optimized to complement the actual energy available. Also, this study showed that obtaining consistent material properties for the conductive concrete overlay panels is a challenge. Therefore, future systems should consider using prefabricated conductive overlay panels batched under controlled environment conditions. The thermal mass properties of the overlay panels are limited. Because of the large exposed surface area of the test mats, the conductive concrete overlay panels were unable to maintain constant temperature.

The UA research team also explored a preliminary system using surface heat wires protected by an epoxy sealant, and solar energy to develop an anti-icing pavement surface. The system uses the same solar energy supply as the conductive concrete system; the difference lies in the area that the electric energy is required to energize. In the previously discussed approach, a larger amount of energy is required to energize a 4-in.-thick conductive concrete mat; conversely, using surface heat wires directs energy to a much more confined area. Early documented results for this approach showed some potential, although additional work would be required to optimize the heat wire configuration within the pavement surface.

1. INTRODUCTION.

Snowy and icy pavement conditions significantly impact airport operations by creating hazardous conditions for aircraft, figure 1. Snow removal efforts can be costly and labor-intensive for airport operators. For example, approximately $4 million is budgeted for airside/runway snow removal at Minneapolis-St. Paul International Airport (MSP). Snow removal typically entails plowing and chemical treatment. Conversely, this study investigates a method to prevent snow/ice accumulation on airfield pavements by maintaining an above-freezing temperature at the pavement slab surface.

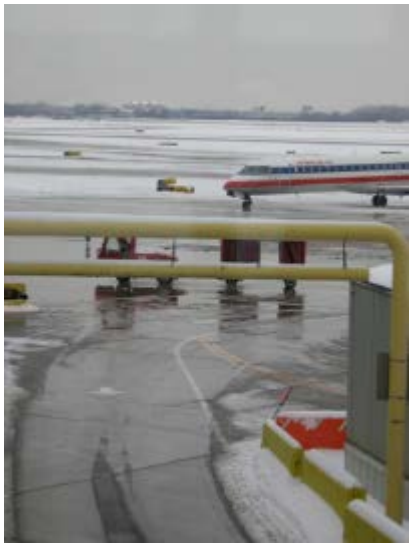

Figure 1. Icy Conditions at O'Hare International Airport; January 21, 2012

Between 1958 and 1993, runway water, ice, or snow contributed to more than 100 airplane accidents [1]. In a more recent study, between January 1978 and January 2009, 100 accidents/incidents (involving jet or turboprop aircraft weighing more than 5600 lb and having a minimum of two engines) occurred at U.S. runways with slush, ice, or snow [2]. A breakdown of the accidents/incidents is given in table 1.

Table 1. Aircraft Overrun Incidents/Accidents With Slush, Snow, or Ice

Overrun Type	Incident	Accident
Landing	67	21
Takeoff	4	8
Total	71	29

To ensure safe aircraft ground movements during winter storm conditions, airport authorities use plows, snow blowers, and/or sweepers to remove snow. For icy conditions, runway deicing fluids are applied to break the bond between ice and pavement. Salt also melts snow and ice; however, applying salt to a runway leads to the detrimental effect of pavement and aircraft landing gear corrosion. As an alternative, more environmentally friendly freezing-point depressant chemicals are used as anti-icing agents to reduce the ice-pavement bond while

complying with U.S. Environmental Protection Agency storm water regulations. Although manually removing snow and applying deicing solvents is one solution, it warrants adequate airport personnel and equipment, which can be costly. Conversely, alternative solutions are available that may be more advantageous. A deicing/anti-icing system that may be appropriate for airfield runways uses conductive concrete. Conductive concrete overlay panels are already in use at a Nebraska bridge site [3]. Energy is supplied to the concrete overlay panels at the Nebraska bridge site using the local energy grid.

The objective of this study was to investigate the suitability of using conductive concrete with a renewable energy source instead of grid energy to power the anti-icing system. Although this approach may be applicable for taxiways, runways, and aprons, it may be most cost-effective within short taxiway sections between adjacent parallel runways where machinery mobility is restricted due to safety.

2. PAVEMENT DEICING SYSTEMS.

Pavement deicing methods can be categorized based on their energy source: chemical, hydronic, and electric. Each system has known advantages and disadvantages, which can include high installation cost, high operational cost, damage to the pavement structure, and damage to the environment. A brief discussion of these methods follows.

2.1 CHEMICAL DEICING SYSTEMS.

Deicing chemicals, including salts, have frequently been used on pavement surfaces. Although this technique is effective, the chemicals used can cause severe, corrosive damage to reinforcing steel within concrete pavements [4 and 5]. Steel reinforcement within a concrete pavement corrodes when exposed to a combination of water and deicers that include chloride and/or acetate. Deicers cause physical and chemical transformations in the cement paste and aggregates, and when used in large amounts, can be environmentally detrimental.

Several different chemical deicing solutions are currently in use. These solutions can be separated into two categories—those containing chloride salts and those containing acetate salts [4]. In 2000, Lee, et al. [5], studied salt effects on concrete during freeze/thaw and wet/dry conditions. When subjected to deicing salts, such as sodium chloride and calcium chloride at low concentrations, the concrete showed relatively minimal deterioration and cracking. Damage caused by these salts appeared to result from the development of crystalline structures within the concrete. Although the concrete displayed greater deterioration at higher concentrations, it was quite low in comparison to deicing chemicals containing acetate.

Other chemicals considered in reference 5 included magnesium chloride and calcium magnesium acetate. Even at low concentrations, magnesium chloride and calcium magnesium acetate resulted in significant concrete damage. Although these chemicals are effective for deicing, over time, they can significantly deteriorate the concrete structure. Deterioration due to magnesium chloride and calcium magnesium is generally due to the formation of brucite [4 and 5]. Brucite is formed when cement paste or concrete is exposed to magnesium concentrations. Brucite is the mineral form of magnesium hydroxide. It is an expansive gel-like material that causes crack development within the concrete structure.

2.2 ALTERNATIVE DEICING SYSTEMS.

Although chemical application is typically used, agencies have investigated alternative deicing approaches. Some U.S. highway departments have installed fixed alternative deicing systems at bridge sites. An early system installed in 1948 by the Oregon Department of Transportation incorporated a geothermal system in the bridge pavement [6]. Heat was distributed through a pipe network cast within the concrete bridge deck slab. However, over time, the pipes experienced heavy corrosion, and in 1998, the grid was replaced during a bridge reconstruction project. Another road deicing technique was developed in the late 1950s in the United Kingdom [7], which entailed using electric heating cables that were embedded into the pavement at the road foundation pavement interface. This method proved very effective by transferring heat from the embedded cables to the slab to melt the ice or snow evenly throughout the concrete slab. An even heat distribution was produced throughout the slab using closely spaced cables in the concrete. The high installation cost of using electric cables was determined to be a major disadvantage.

Minnesota Department of Transportation Districts installed fixed deicing systems on some of their curved and super-elevated bridge decks [8]. This deicing system consists of a chemical storage tank, a pump delivery system, and a grid of sprayers used to apply the deicing solvent. Installation cost of an automatic system on Trunk Highway (TH)61 in Dresbach, MN, was $25,000 in 1998, and annual operation and maintenance costs were approximately $2,000 in 1998. The system can be operated manually at the site or remotely. Another example is the fixed deicing system installed by the Virginia Department of Transportation [9]. This system incorporates fixed automatic spray technology (FAST). In FAST, a liquid-chemical, freezing-point depressant, magnesium chloride is sprayed through a grid of nozzles. In addition to the nozzle grid, the system includes an anti-icing fluid reservoir and a pump. The installation cost for the system was approximately $60,000 in 2004.

Research is currently being conducted on heat pipe exchangers, heat pumps, and geothermal heat pipes. Heat pipe exchangers are used in China as a way to prevent ice and snow accumulation [10]. This repeatable process uses a fluid that evaporates when heated and condenses into liquid form when cooled. The heated fluid rises to the top of the heat exchange pipe that is embedded within a concrete pavement, where heat energy is transferred from the heat exchange pipe to the pavement. Once the heat transfer is complete, the evaporated liquid condenses to tiny droplets that fall to the bottom of the pipe due to gravity. Ammonia is commonly used for the liquid because it does not freeze in the considered temperature range. The primary disadvantage to this process is the high construction costs from the drilling process and pipe assembly.

Most recently, the Federal Aviation Administration is involved in a research project at Binghamton University in New York to implement a radiant geothermal heating system. This geothermal heating system pumps water underground to absorb the earth's natural geothermal energy. This energy is then pumped through a pipe system to distribute the energy uniformly through the runway pavement [11].

2.3 CONDUCTIVE CONCRETE DEICING SYSTEM.

Some of the deicing/anti-icing systems previously described require mechanical pumping and fixed equipment located near the pavement region, which would be unacceptable within the runway safety area of an airfield. Therefore, conductive concrete provides a deicing/anti-icing system that is more applicable to airfield pavements [12]. Research conducted for the Nebraska Department of Roads investigated the use of conductive concrete for bridge deicing and anti-icing. In the study conducted by the University of Nebraska–Lincoln, a concrete deck mix was developed using conductive concrete with an electrode grid [7]; however, the mix developed in the study is proprietary. When the electrode grid is connected to an external electric power source, the conductive concrete bridge material generates enough heat to prevent ice from forming on the bridge deck.

2.4 CONDUCTIVE CONCRETE CASE STUDY.

A conductive concrete overlay was installed at the Roca Bridge in Lincoln, Nebraska. Roca Bridge is a three-span highway bridge, 150 ft long, and 36 ft wide [3]. The 4-in.-thick conductive concrete overlay was installed within a 117- by 28-ft section overlaying a 10-in.-thick concrete slab. The conductive concrete overlay was subdivided into panels to improve heat conduction. Each 4-in.-thick panel was 4 by 14 ft. In addition to providing electrical conductivity, the conductive concrete overlay had to satisfy minimum bridge deck strength requirements and provide material workability during concrete placement. The concrete mix compressive strength was approximately 4500 psi with a 145 pcf unit weight. A preliminary mix design, developed by Tuan, was comprised of 20% steel shavings and 1.5% steel fibers by volume percentage [7]. However, steel shavings are an industrial waste that had to be cleaned before they were added to the concrete mix. Consequently, the mix was later modified to replace the 20% steel shavings with 15% carbon particles to eliminate the need for cleaning and to improve the aggregate size consistency within the concrete [3]. The specific details of this modified conductive concrete mix are proprietary.

In the Roca Bridge conductive concrete panel, heat energy originates at electrodes implanted within each panel. Two 3-1/2 by 3-1/2 by 1/4 steel angles are used as the electrodes. The two angles are separated by 3.5 ft and run parallel to the 14-ft panel side. Each angle is attached to an outside electrical source, a nearby grid electric line: a three-phase, 600-amp, 220-volt alternating current (AC) power supply. Heat is generated via the electric resistivity of the conductive concrete overlay panel through Joule heating. Tuan compared the use of AC and direct current (DC) power supplies [7] and found that the AC power supply heated the slab panels more uniformly and had lower operating costs than DC power supply. During the deicing operation, power supplied to the overlay was limited to 10 amps.

The unit area construction cost for the overlay was $\$59/ft^2$. Over a 50-month period (December 2003-February 2008), the average electric energy consumed per storm in overlay heating was 0.916 kW-hr/ft^2 per storm. Considering an energy cost of \$0.08/kW-hr, the cost per storm to prevent icing was $\$0.074/ft^2$.

3. CONDUCTIVE CONCRETE MIX.

3.1 MIX DESIGN.

The critical material parameter in describing a concrete's suitability as a conductive concrete is the material's electrical conductivity. Typically, concrete's electrical resistivity, which is the reciprocal of conductivity, is in the range of 6 to 11 kΩ•m [13]. In comparison, the electrical resistivity of the conductive concrete mix developed by Tuan [3] in an earlier study was 0.003 to 0.005 kΩ•m. Generally, concrete consists of cement, fly ash, sand, and limestone. Conversely, in a conductive concrete mix, the sand fine aggregate is replaced in part with a fine, electrically conductive material. Preliminary mixes used steel shavings; however, because steel shavings are waste products that require cleaning prior to usage and because they exhibit high variability, graphite powder was substituted for the steel shavings to improve conductivity [14].

A conductive concrete mix design using graphite powder and steel fibers is presented in reference 12. However, the mix is proprietary, and therefore, the mix details are nondescript. Consequently, the University of Arkansas (UA) researchers developed a conductive concrete mix design based on strength, conductivity, and workability specifically for this study. Ten trial mix batches were tested and compared to optimize material behavior for this study, table 2. Compression tests were conducted at 28 days using 4-in.-diameter, 7-in.-long cylinders. Type I cement, Class C Fly Ash, coarse aggregate with a 1/2-in. maximum aggregate size, fine aggregate using river sand with a fineness modulus of 2.50, and ADVA® Cast 575 Superplasticizer (high-range water reducer, HRWR) were typically used in these mixes.

Replacing sand fine aggregate with graphite powder adversely affected the mix workability. To ensure adequate compressive strength, the water/cement ratio (w/c) was fixed at 0.4. Consequently, an HRWR was added to keep the w/c at 0.4 and to improve the mix workability. The initial conductive concrete mix design used 6 fluid ounces of HRWR per 100 lb of concrete. Although this amount of HRWR gave a 3.5-in. slump, higher amounts were considered to determine an upper bound dosage without compromising the concrete compressive strength.

Table 2. Trial Mix Batches

MIX	GRAPHITE POWDER (%)	RAPHITE POWDE DESIGNATION	STEEL FIBER 38 mm (1.5") (%)	CEMENT (TYPE 1) (%)	FLY ASH (%)	COARSE AGGREGATE (%)	FINE AGGREGATE (%)	WATER (%)	AIR (%)	w/c
1	24.9	A60,A99,A625	1.5	15.1	5.4	26.6	0.8	23.7	2.0	0.40
2	24.9	A4012	1.5	15.1	5.4	26.6	0.8	23.7	2.0	0.40
3	19.9	A4015	1.5	15.1	5.4	26.6	5.8	23.7	2.0	0.40
4	19.9	A4071	1.5	15.1	5.4	26.6	5.8	23.7	2.0	0.40
5	19.9	A4071	2.5	15.1	5.4	26.6	4.8	23.7	2.0	0.40
6	19.9	A4071	3.5	15.1	5.4	26.6	3.8	23.7	2.0	0.40
7	17.2	A4071	5.0	15.1	5.4	26.6	5.0	23.7	2.0	0.40
8	17.2	A4071	2.7	15.1	5.4	26.6	7.2	23.7	2.0	0.40
9 BFS	7.2	A4071	2.7	11.9	0.0	36.1	21.4	18.7	2.0	0.35
10 BFS	17.2	A4071	2.7	18.8	0.0	31.0	4.5	23.7	2.0	0.40
11	17.2	A4071	2.7	15.1	5.4	26.6	7.2	23.7	2.0	0.40

MIX	UnWt (pcf)	UnWt (kN/m^3)	f'c (ksi) 28 day	f'c (MPa) 28 day	El. Resistivity (ohm-in) 28 day	El. Resistivity (ohm-cm) 28 day
1	137.1	21.6	2.75	18.95		
2	137.1	21.6	3.10	21.36		
3	138.3	21.7	4.15	28.59		
4	138.3	21.7	5.60	38.58		
5	137.4	21.6	5.10	35.14		
6	136.4	21.4	na	na		
7	135.6	21.3	na	na		
8	137.8	21.7	5.85	40.31	253	643
9 BFS	133.8	21.0	4.80	33.07	1778	4516
10 BFS	129.6	20.4	5.70	39.27	711	1806
11	137.8	21.7	6.15	42.37	156	396

Each mix used steel fibers and graphite powder to improve the conductivity of the material. In the conductive concrete mix, 1.5-in.-long, low-carbon, cold drawn steel wire fibers were used, as shown in figure 2. The steel fibers were purchased from Propex™. Specifications for the steel fibers are listed in table 3 and are ASTM A820-compliant [15].

Figure 2. Trial Mix Batches

Table 3. Steel Fiber Properties

Fiber Length	1.5 in.
Equivalent Thickness	0.045 in.
Tensile Strength	140 - 180 ksi
Aspect Ratio	34

Graphite is an allotrope of the chemical element carbon. Allotropy is the property of a chemical element to occur naturally in two or more forms. The most stable carbon form is graphite. It is considered the highest grade of coal. Graphite is a naturally occurring semimetal, which makes it a strong electrical conductor. There are three main types of graphite: crystalline flake graphite, amorphous graphite, and vein graphite. Of the three types, the crystalline flake graphite is the most common. The crystalline flake graphite, shown in figure 3, when added to the conductive concrete mix with steel fibers, creates electrical conductivity.

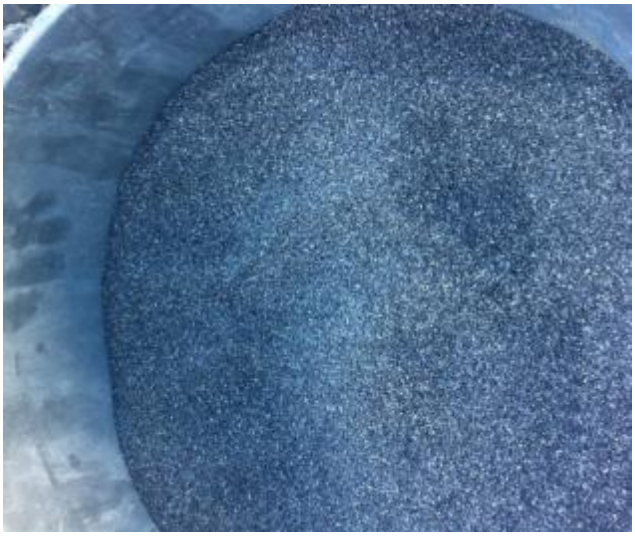

Figure 3. Sample of A4071 Graphite Powder From Asbury Carbons

Sample trial sizes for the graphite powder were provided by Asbury Carbons and ranged from 44-850 microns. Figure 4 shows a sieve analysis for each graphite powder considered during this study for trial batching.

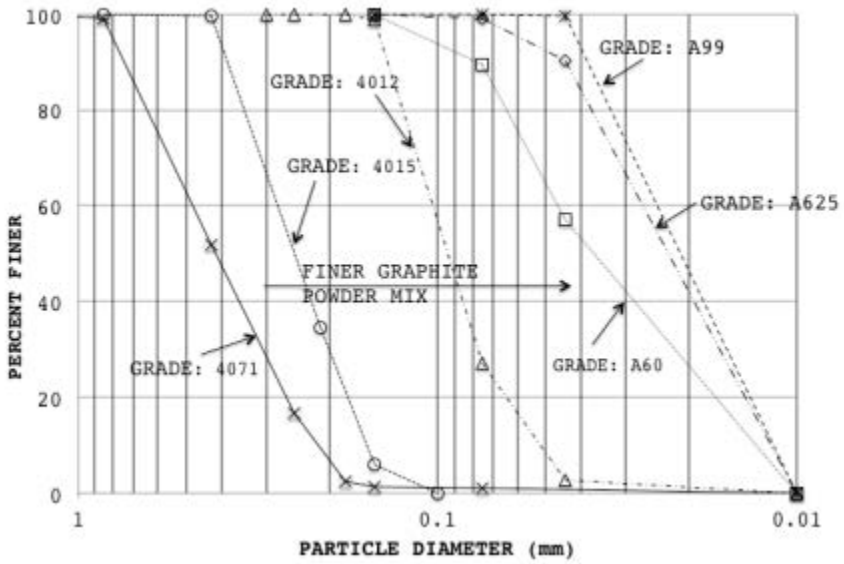

Figure 4. Graphite Powder Gradation

At the start of this study, the graphite powder gradation best suited for the conductive concrete mix was unknown. In preliminary batching, the conductive concrete mix was found to be highly sensitive to the coarseness of the carbon particles in the graphite mix. Graphite powder absorption decreased as the graphite powder aggregate size increased. Consequently, mix design strength increased as the graphite powder aggregate size increased. In trial mix 1, table 2, a fine graphite powder using equal percentages of Grade A60, A99, and A625, as shown in figure 4, was tried. This very fine graphite powder mix resulted in a high water demand. As a result, a significant water volume was warranted during mixing to improve workability; however, adding water negatively impacted compressive strength. The results of the trial mix 1, 14-day compression test are shown in figure 5.

Figure 5. Trial Mix 1, 14-Day Compression Test

Trial mix 2, table 2, used a graphite powder consisting of coarser carbon particles (97.2% carbon particles >44 microns), figure 4. Workability improved as well as compressive strength, figure 6 and table 3.

Figure 6. Trial Mix 2, 7-Day Compression Test

Two additional batch mixes, trial mix 3 (93.9% carbon particles >150 microns) and trial mix 4 (97.3% carbon particles >180 microns), were tested, with each mix having a larger graphite

powder carbon particle size. Increasing graphite particle size improved workability, and trial mix 3 showed an increase in the 7-day compressive strength, figure 7 and table 4.

Figure 7. Trial Mix 3, 7-Day Compression Test

Table 4. Compressive Strength

Trial Mix	Test	f'c (psi)
2	1	1650
2	2	1800
3	1	2950

Table 5 details the trial mix 4 concrete mix design using the 250- to 850-micron graphite powder (A4071). Graphite powder mix A4071 created the best mix blend and therefore was used in trial mixes 4 through 11, table 2.

Table 5. Conductive Concrete Mix Proportions

Trial Mix No.	4		8		10	
Mix Material	Weight (lb/yd^3)	Volume (%)	Weight (lb/yd^3)	Volume (%)	Weight (lb/yd^3)	Volume (%)
Steel Fiber	30	1.6	50	2.7	50	2.7
Cement	800	15.1	800	15.1	630	11.9
Fly Ash	200	5.4	200	5.4	0	0
Coarse Aggregate	1300	26.6	1300	26.6	1400	36.1
Fine Aggregate	456	10.3	319	7.2	948	21.4
Water	400	23.7	400	23.7	315	18.7
Air	n/a	2.0	n/a	2.0	n/a	2.0
Graphite Powder	575	15.2	650	17.2	270	7.2

n/a = Not applicable

A core sample of trial mix 4 is shown in figure 8, and a microscopic view of the hardened mix is shown in figure 9. Figure 9 identifies minimal steel fiber. Consequently, conductivity for trial mix 4 was low.

Figure 8. Trial Mix 4, 1.6% Steel Fiber, 15.2% Graphite Powder

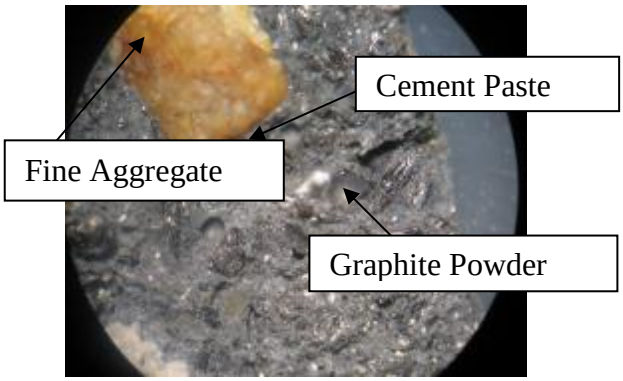

Figure 9. Microscopic Image of Trial Mix 4

A series of mixes were developed that increased the steel fiber percentage from 1.6% to 3.5% (trial mix 5), 4.5% (trial mix 6), and 5% (trial mix 7). However, increasing the steel fiber percentage reduced workability; therefore, a mix with 2.7% steel fiber and 17% graphite powder (trial mix 8 in table 2) was finally developed to improve conductivity while also providing good strength and workability characteristics. The additional steel fiber is evident in trial mix 8, figure 10, compared to trial mix 4, figure 8. The electrical resistivity for trial mix 8, as shown in table 2, was measured using a 2.5- by 13- by 18-in. conductive concrete mat with two embedded #8 reinforcing bars as electrodes running parallel to the 18-in. mat length.

Figure 10. Trial Mix 8, 2.7% Steel Fiber, 17% Graphite Powder

Blast furnace slag (BFS), as a limestone aggregate replacement, was the last material to be investigated in the conductive concrete mix evaluation. BFS is a by-product of steel production. In some productions, BFS contains highly conductive iron residue along its surface. In reference 7, it was reported that BFS could completely replace all coarse and fine aggregate and, therefore, allow a smaller amount of graphite powder to be used to achieve a more conductive mix design. The Edward C. Levy Company donated the BFS used in this study. Table 2 shows the results of replacing coarse and fine aggregate with BFS in trial mixes 9 and 10. Trial mix 9 used BFS with 7.2% graphite powder, figure 11. In trial mix 10, the graphite powder was increased from 7.2% to 17.5%. After compression testing, it was concluded that while the compressive strength of the BFS concrete was comparable to conventional aggregate concrete, the conductivity did not improve. Consequently, BFS was not considered in the remaining mixes for this study. Instead, coarse limestone aggregate was used for the large-scale test mat mix. Trial mix 11 repeated the material mix of test mix 8 to validate the test mix 8 results using limestone aggregate.

Figure 11. Trial Mix 9, BFS, 7.2% Graphite Powder, and 2.5% Steel Fibers

3.2 HEAT FLOW AND CONDUCTIVITY TESTS.

Heat flow and conductivity were measured using 2.5- by 13- by 18-in. small test mat samples, figure 12. Steel reinforcing bars (No. 8 or No. 10) were used as electrodes to supply DC voltage to the conductive concrete sample. The electrodes were spaced at approximately 10.5 in. A multimeter across the electrodes was used to measure the electric resistance for trial mixes 8 through 11. It was then converted to an electrical resistivity value based on the sample thickness and electrode spacing. Concrete's typical electrical resistivity is in the 236 to 433 kΩ•in. (6 to 11 kΩ•m) range [13]. Conversely, trial mix 11 had an electrical resistivity of 0.156 kΩ•in. (0.004 kΩ•m), 1/1513 of conventional concrete.

Figure 12. Test Overlay for Measuring Heat Flow

Electrical resistivity is measured by applying a known current, *I*, to two spaced electrodes that are embedded in the material under analysis. Using Ohm's Law, the resistance, *R*, is determined from the drop in voltage, *V*, over the length of the specimen:

$$R = \frac{V}{I} \tag{1}$$

The electrical resistivity is a material property and independent of the structure geometry. It is determined from the test electrical resistance, *R*, as:

$$\rho = R\frac{A}{L} \tag{2}$$

where ρ is the material's average electrical resistivity, *L* is the electrode spacing, and *A* is the cross-sectional area of the test material parallel to the electrodes through which the current flows.

For the heat flow tests, a thermocouple was located at the center of the test slab to monitor surface temperature, figure 13.

Figure 13. Heat Flow Monitoring

The heat flow test results for trial mix 8 (limestone aggregate) and trial mix 10 (BFS) are shown in figure 14. As input voltage increased, maximum slab temperature and temperature gradient increased. As figure 14 shows, substituting the limestone coarse aggregate with BFS did not improve conductivity behavior. Trial mix 10 with BFS warranted 80 volts input before developing a noticeable temperature gradient. Consequently, limestone coarse aggregate was used in subsequent conductive concrete mixes for this study.

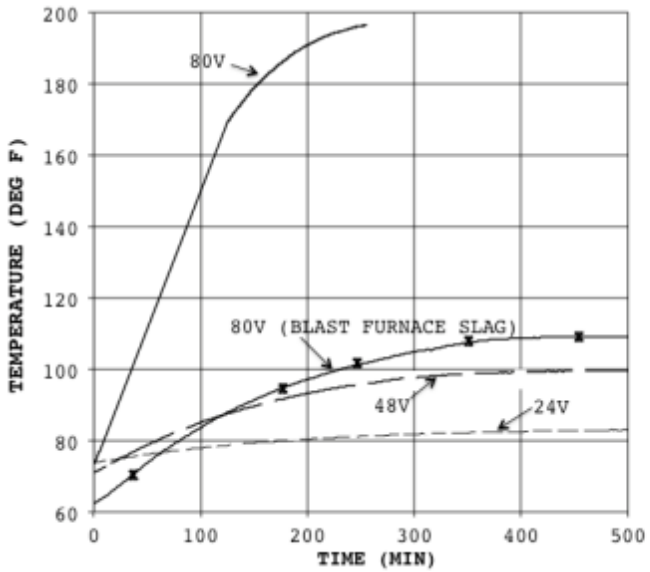

Figure 14. Temperature Gradient for Trial Mix 8, Limestone Coarse Aggregate (24V, 48V, and 80V) and Trial Mix 10, BFS Coarse Aggregate at 80V

3.3 EFFECTS OF HYDRATION ON CONDUCTIVITY.

Concrete hydration occurs when water comes in contact with cement to form a cement paste bond between aggregates. Cement particles within concrete hydrate when water is available. Concrete reaches 90% of its maximum compressive strength at approximately 28 days. Therefore, at 28 days, most of the moisture in the concrete has either reacted with the cementitious material or has evaporated, leaving voids within the concrete matrix. As moisture within the concrete decreases over the 28 days, concrete conductivity also decreases. Conductivity decreases fairly quickly the first few days, and then decreases at a slower rate. Figure 15 demonstrates the effect of hydration on resistivity over time.

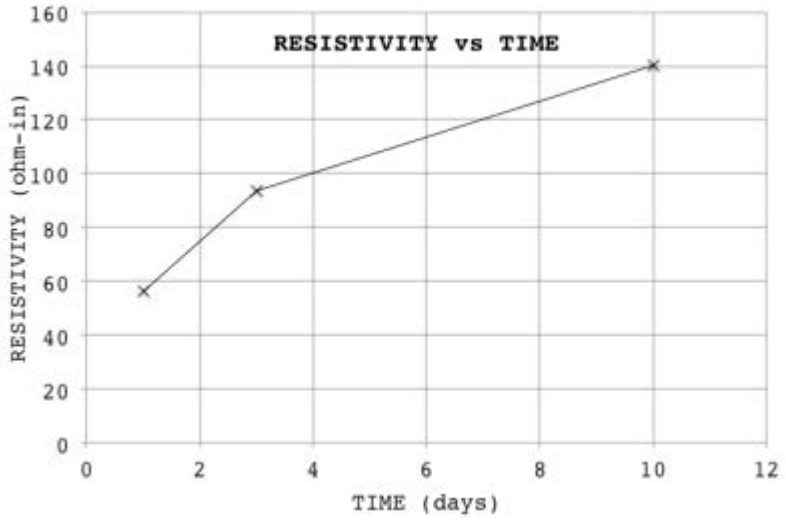

Figure 15. Electrical Resistivity as a Function of Age

3.4 POWER DENSITY.

Based on the trial mix 11 electrical resistivity (156 Ω-in.), power density was calculated to optimize supply voltage and electrode spacing as a function of cost and derived power density, figure 16.

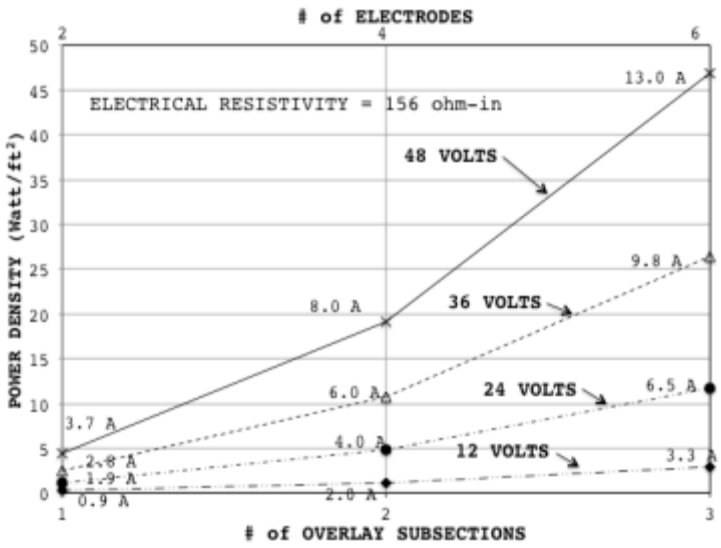

Figure 16. Power Density for a 4- by 10-ft Conductive Concrete Overlay Panel (ρ = 156 ohm-in.)

The voltages shown in figure 16 are in multiples of 12 since 12 DC-V batteries were used for the project energy storage system. In figure 16, the subsections are shown at equal spacing. The edge electrodes are assumed to be 4 inches from the edge surface. Between the edge electrodes, the space is subdivided equally, depending on the number of overlay subsections within the panel. Each internal subdivision has two electrodes separated by 3 inches. The same electrical polarity is used at each of the closely spaced electrodes to control the current path between a negative and positive electrode set. For each case, the corresponding amperage is superimposed on figure 16. In the work performed by Tuan [3], the average peak power delivered to the overlay panels was 42 W/ft^2 for deicing during snowstorms. In Tuan's work [3], energy was supplied shortly before a snowstorm. Energy in this study was supplied continuously to the overlay panel in an attempt to keep the pavement at an above-freezing temperature. Consequently, a lower average peak power was used. The electrical resistivity is temperature sensitive. A temperature increase is accompanied by an electrical resistivity decrease and an increase in electrical conductivity. Tuan found that conductive concrete experiences an increase of electrical resistivity of four times between 25° and 100°F [7]. For this study, the electrical resistances of the small test mats were measured at room temperature. To simulate behavior at subfreezing temperature, power density was calculated for an electrical resistivity three times the electrical resistivity at room temperature (468 ohm-in.), figure 17. A comparison of figures 16 and 17 illustrates the sensitivity of the power density to electrical resistivity.

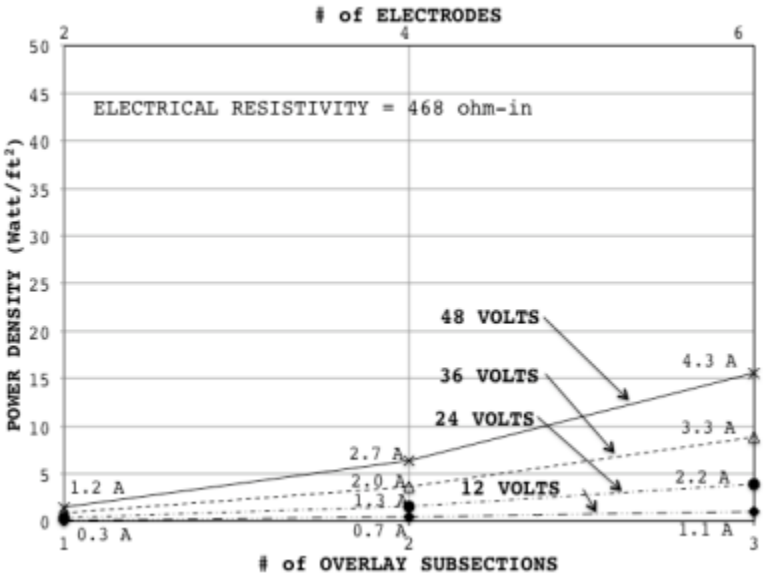

Figure 17. Power Density for a 4- by 10-ft Conductive Concrete Overlay Panel (ρ = 468 ohm-in.)

4. TEST MAT CONSTRUCTION.

A 20- by 20-ft conductive concrete test mat was constructed at the UA Engineering Research Center to investigate the suitability of using conductive concrete overlay panels coupled with solar energy to develop an anti-icing pavement. A plan view and elevation view of the test mat are shown in figures 18 and 19, respectively. The plan view, figure 18, shows the test mat size as 20 by 24 ft, which includes two additional 4- by 10-ft panels. These two additional panels were made using a conventional concrete mix to provide a basis for comparing results with the conductive concrete panels.

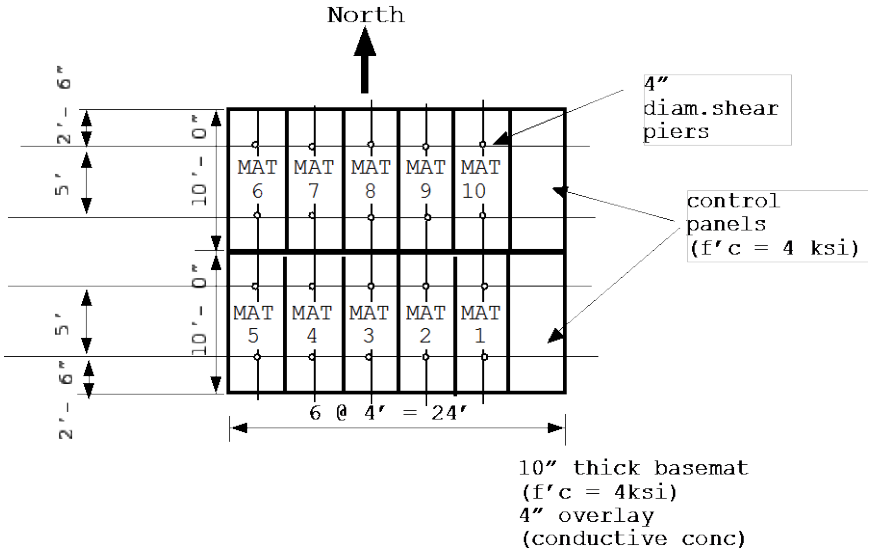

Figure 18. Test Mat Plan View

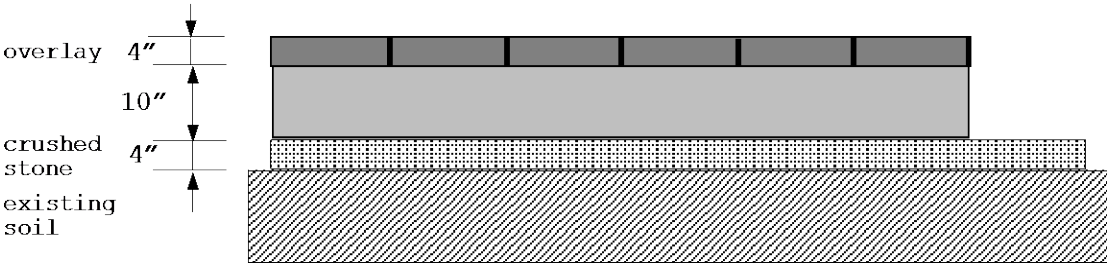

Figure 19. Test Mat Elevation View

The elevation view in figure 19 shows a 4-in.-thick crushed stone layer under the test mat. A 4-in.-thick crushed stone layer was placed over a 65- by 65-ft area to ensure a secure base for experimental construction. The area was left unfenced to provide easy truck access to the test mat. After the 10-in. base mat was placed, a fence was installed to secure the 65- by 65-ft area, figure 20.

Figure 20. The Secured 65- by 65-ft Test Area for Anti-Icing Experimentation

Formwork was constructed for the entire 14-in. test mat thickness, figure 21. Wood separators positioned on the hardened 10-in. base mat were needed to develop the individual conductive concrete overlay panels. A 4-ksi concrete was used for the 10-in. base mat.

Figure 21. Test Mat Formwork

Figure 22 shows the 10-in. base mat after pouring. The top surface of the base mat was left unfinished to improve interaction between the 10-in. base mat and 4-in. overlay.

Figure 22. Test Mat Placement

The orange cylinders visible in figure 22 were positioned before the base mat was poured to create 4-in.-diameter cavities for shear piers, as designated in figure 18. The shear piers were incorporated to improve interaction structurally and thermally between the overlay and base mat. Figure 23 shows the shear pier cavities created in the base mat prior to placement of the conductive concrete overlay. Concrete specimens were taken when the 10-in. base mat was poured to validate its 4-ksi compressive strength.

Figure 23. A 4-in.-Diameter Shear Pier Cavity

5. CONDUCTIVE CONCRETE OVERLAYS.

5.1 CONDUCTIVE CONCRETE MIX PROCEDURE.

Trial mix 11 was used as the conductive concrete mix for the full-scale overlay test mat. The 4- by 10-ft overlay panel grid network was constructed using 2- by 4-in. wood studs. In addition to providing support while placing the concrete, the wood studs create an insulated barrier between adjacent overlay panels. The conductive concrete was mixed at the concrete laboratory facilities of the UA Engineering Research Center Facility in Fayetteville, Arkansas. The concrete rotary mixer was then moved to the large-scale test mat site and the conductive concrete placed on the existing 10-in., normal-weight concrete base mat.

The conductive concrete was batched using the following procedure:

1. The inside of the concrete mixer was sprayed with water and drained to allow materials to mix well and not accumulate on the mixer wall.

2. Coarse and fine aggregate were added to the concrete mixer.

3. Steel fibers were added to the aggregate mix.

4. Graphite powder was then added to the dry mix.

5. Half of the total required water was added to the dry materials.

6. Cement was added to the mix.

7. Silica fume was then added to the concrete.

8. An HRWR was added to the unmixed water. The HRWR-water mix was then added to the concrete mix.

9. Mixing continued for a minimum of 20 minutes before the conductive concrete was placed in the overlay panel formwork.

For the large-scale test mat, a total of 17 cu. ft. of conductive concrete was batched for each individual 4-in. by 4- by 10-ft overlay panel.

5.2 TEST OVERLAY 1.

Batching and experimentation for the large-scale overlay test mat began in early July 2011. Trial mix 11, table 2, was used for the first 4-in. by 4- by 10-ft conductive concrete overlay test panel. The concrete was batched using a 9.5 ft^3 rotary drum mixer. Because of the mixer size, the concrete mix was batched in three individual sets and taken to the test site location to be uniformly placed. During this batching process, the first batch of concrete did not have any steel fibers while the second and third batches had higher than 2.7 percentages to attain an average 2.7% for the entire mix. This approach for the first overlay panel was used to observe whether or not the steel fibers would severely decrease the concrete workability on a large-scale mix. The mix workability and ease of finish were comparable to conventional concrete, as shown in figure 24.

Figure 24. Finish of Electrical Conductive Concrete

Each conductive concrete lift was placed individually in a horizontal layer with the subsequent lift overlaying the previous lift. A concrete vibrator was used to ensure uniformity and full contact between the concrete and the electrodes. Although the concrete vibrator achieved a strong bond between concrete and electrodes, the uniformity of the concrete suffered. Since the concrete was not placed in a single pour, the mat section closest to the concrete pour spout, south end, received a higher steel fiber concentration. This problem was corrected in subsequent pours when a larger concrete mixer, 1.5 yd^3, was available for use. Consequently, only a single concrete batch was required for each following overlay panel. After completing the concrete pour, a tarp was placed to cover the mat to minimize thermal shrinkage cracking.

The electrode configuration for Test Overlay 1 is shown in figure 25. The equal electrode spacing was used to examine optimal electrode spacing with respect to power consumption and heating capabilities.

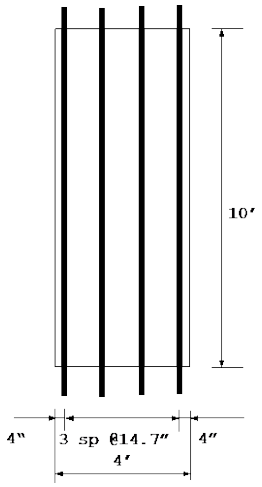

Figure 25. Test Overlay 1 Electrode Configuration

5.3 TEST OVERLAY 2.

Test Overlay 2 was batched and poured on August 25, 2011. The concrete mix design for Overlay 2 was identical to Test Overlay 1. Test Overlay 2 and subsequent concrete pours were batched using a 1.5-yd^3 rotary drum mixer. Differences between Test Overlays 1 and 2 correspond to the electrode spacing. Test Overlay 2 had an electrode configuration where the two outside electrodes were located 4-in. from each test panel edge and the inside electrodes were separated by 3 inches. Figure 26 shows the electrode configuration for Test Overlays 2 through 10.

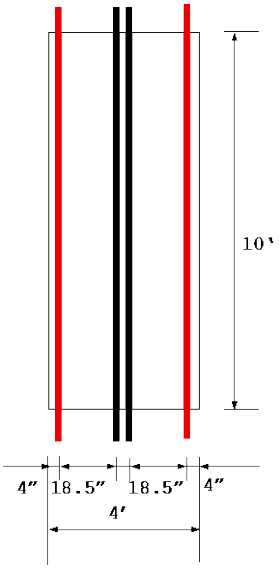

Figure 26. Test Overlays 2 Through 10 Electrode Configuration

This configuration was to obtain a more uniform heat distribution throughout the concrete panel by allowing the current to flow through two subsections of the concrete slab. Current through a material is directly related to electrode spacing, as shown in figures 16 and 17. Therefore, the

increased spacing used in Test Overlay 2 reduces the current through the concrete material. Figure 27 demonstrates how the electrodes were placed prior to concrete pouring.

Figure 27. Test Overlays 2 Through 10 Electrode Spacing

The concrete mix for Test Overlay 2 had a larger slump than Test Overlay 1. The concrete vibrator was not used on Test Overlay 2 because of the slump increase; it was assumed that the concrete would flow uniformly when placed and would adequately encase the electrodes. However, Test Overlay 2 concrete borings revealed that there was insufficient contact between the concrete and electrodes. Figure 28 shows the poor contact at the concrete/electrode interface. This lack of contact surface between the electrodes and concrete resulted in poor concrete conductivity performance for Test Overlay 2.

Figure 28. Contact Between Concrete and Electrode for Test Overlay 2

Test Overlay 2 was not covered with a tarp after the concrete was poured. Consequently, after several days of curing, thermal cracks appeared. Figure 29 shows that the thermal cracks found in Test Overlay 2 occurred throughout this overlay panel.

Figure 29. Shrinkage Cracks in Test Overlay 2

Cores taken from Test Overlay 2 showed that the thermal shrinkage cracks were not limited only to the surface, figure 30. Consequently, these cracks created barriers for the electric current flow resulting in a very high material electrical resistance.

(a) Elevation View

(b) Top View

Figure 30. Core From Test Overlay 2

5.4 TEST OVERLAY 3.

Test Overlay 3 was batched and poured on September 29, 2011, with the same electrode spacing as Test Overlay 2. To remedy conditions that caused the poor conductivity in Test Overlay 2, a concrete vibrator was used during placement and the mat was covered with a tarp after finishing.

After Test Overlays 1 and 2 were placed, it was concluded that a larger slump would be advantageous to improve the contact interface between the electrodes and concrete. To keep compressive strength and conductivity constant, the HRWR was increased to improve workability. The HRWR was increased from 6 to 9 ounces per 100 lb of concrete. The HRWR increase resulted in a definite slump increase and improved workability. After the concrete was placed, some water bleeding at the surface was observed. Aggregate segregation and material non-uniformity are major concerns with high HRWR dosages and manifest through reduced compressive strength. During compression tests, slight segregation between the rock and conductive material was observed. Figure 31 shows the Test Overlay 3 slump test with the increased HRWR.

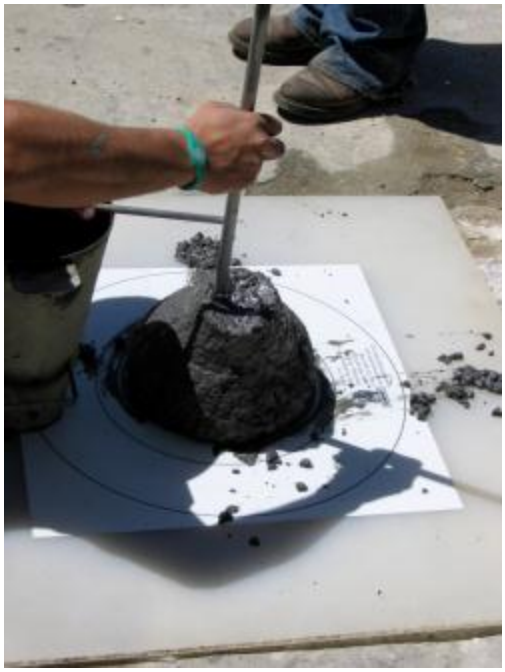

Figure 31. A 4-in. Slump for Test Overlay 3

5.5 TEST OVERLAY 4.

Test Overlay 4, figure 18, was poured on October 13, 2011. This slab was identical to Test Overlay 3 except for the HRWR dosage. For Test Overlay 4, the HRWR dosage was decreased from 9 to 7.5 ounces per 100 lb of concrete. Compared to the compressive strengths of Test Overlays 1 and 2, the compressive strength for Test Overlay 3 was slightly lower at 4700 psi.

During compression tests, test cylinders were monitored for aggregate distribution and aggregate segregation, comparing the top, middle, and bottom of each cylinder. Figure 32 shows an example of the Test Overlay 4 cylinder. It is notable that the cylinder base contains a higher coarse aggregate density.

Figure 32. Aggregate Segregation

5.6 TEST OVERLAY 5.

Test Overlay 5 was batched and placed on November 4, 2011. The conductive concrete mix design was unchanged and the amount of HRWR used was 7 ounces per 100 lb of concrete. The workability and ease of finish for Test Overlay 5 was equal to or better than conventional weight concrete.

5.7 TEST OVERLAYS 6 AND 7.

Test Overlays 6 and 7 were placed on November 11, 2011. Using a 1.5-yd^3 rotary mixer enabled Test Overlays 6 and 7 to be batched concurrently. The HRWR concentration used was consistent with Test Overlay 5. Mechanical properties were measured and averaged for both test mats.

5.8 TEST OVERLAYS 8 AND 9.

Test Overlays 8 and 9 were batched and placed on November 18, 2011. Mechanical properties were measured and averaged for both mats. HRWR dosage was consistent with the previous three test mats.

5.9 TEST OVERLAY 10.

Test Overlay 10 was batched and placed on December 1, 2011. Test Overlay 10 included an increase in steel fibers from 2.7% to 4.5% by volume. The steel fiber percentage was increased to improve material conductivity and as a result of the good workability in the previous test mats.

The compressive strength of Test Overlays 5 through 10 consistently ranged from 5-6 ksi. The measured electrical resistivity for Test Overlays 5 through 10 was in the range of 130 to 665 Ω-in.

All 10 test mats were placed before the Arkansas winter season to enable monitoring of the test mat behavior during winter conditions. Unfortunately, because of the mild 2011-2012 winter, overall test mat behavior during inclement weather was not recorded.

6. PHOTOVOLTAIC ENERGY SYSTEM.

6.1 INTRODUCTION.

Photovoltaic (PV) energy systems obtain renewable energy by converting solar radiation into DC electricity [16]. Light-sensitive diodes, or solar cells, are used in an array configuration to comprise a complete solar panel. When solar radiation enters a solar cell, the photons provided by the radiation energize the electrons within the solar cell to a higher state of energy. The energized electrodes produce DC electricity, which can either be used for immediate usage or stored in an energy storage system for later usage. An individual solar cell can produce approximately 0.5 volts of DC electricity.

An inverter is used in home solar energy applications to convert DC electric energy from the PV cells into the more conventional AC electric energy typically used for home appliances. However, in this study, a DC-AC inverter was not used. Instead, DC energy was supplied directly to the conductive concrete panels negating the need for an inverter. Since the system is independent of an outside energy source, no energy costs and no grid line extension costs were incurred. The PV system components for DC energy are shown in figure 33. The PV array converts sunlight into DC energy. The PV array is comprised of a group of PV cells used to generate electricity. The size of the PV array and the number of panels required are determined based on the estimated energy load and available sunlight at the site location. The battery bank stores energy for use during times when daylight is unavailable. Based on the battery storage bank rating, the system continues to supply energy to the DC appliance when sunlight energy is unavailable. The amp-hour rating required for the battery storage bank is determined by the energy draw of the attached appliances and battery voltage. To maximize battery life, battery discharge is limited to a percentage of the battery capacity. The PV system control/regulator regulates energy generated by the PV array and directs the energy to the appliances or the battery storage bank, or from the battery storage bank to the appliances.

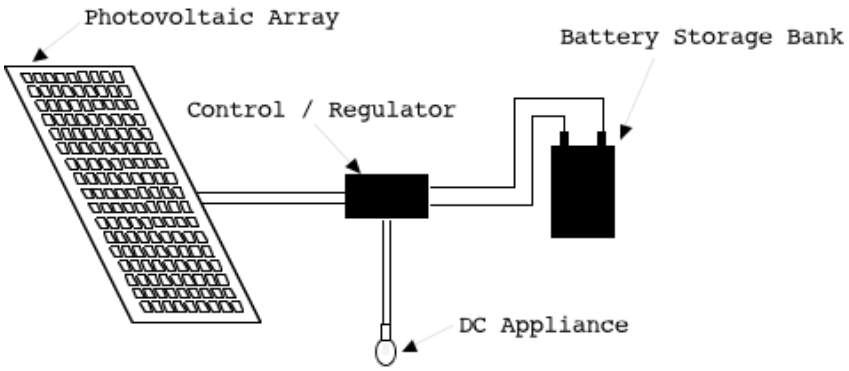

Figure 33. The PV Generating and Storage System

The anti-icing pavement in this study incorporated solar energy to generate heat within the overlay panels. The solar energy was supplied as a DC current to the embedded electrodes within the conductive concrete panels. The PV system components for the DC energy used in this study are shown in figure 34. The PV system control/regulator regulates the energy generated by the PV array and prevents voltage overload to the battery storage bank. The battery storage bank stores excess energy for use when sunlight is unavailable. Based on the battery storage amp-hour bank rating, the system can continue supplying energy for a limited time without sunlight energy.

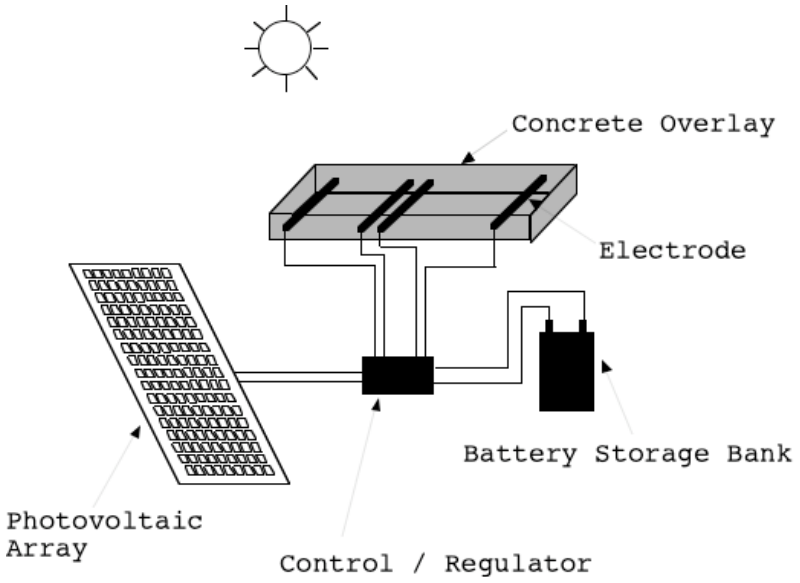

Figure 34. A PV Conductive Concrete Anti-Icing System

The PV system components necessary to supply an immediate energy surge to support pavement deicing are cost-prohibitive. Therefore, the intrinsic characteristics of concrete as a thermal mass together with the zero electric energy cost are to be considered for this study. The thermal mass property of concrete enables the concrete slab to absorb large amounts of heat from ambient temperature conditions that can be combined with heat provided by the PV energy system. This energy is stored within the concrete pavement and later released when there is a temperature

drop. Energy from the PV array is continually supplied to the battery storage bank during daylight. Additionally, energy from the battery storage bank is continually supplied to the overlay panels day and night as needed. In this energy arrangement, energy is introduced into the concrete overlay pavement system continually; however, it is introduced gradually rather than as a power surge immediately prior to a predicted winter storm. Although the system is energy inefficient, solar energy's zero cost makes this inconsequential.

6.2 THE PV ENERGY SYSTEM.

The electrical resistance of the overlay panel, *R*, is a function of the conductive concrete electrical resistivity (ρ); the product of the 120-in. mat length and the 4-in. mat thickness (*A*); and the distance between electrodes (*l*):

$$R = \rho \frac{l}{A} \tag{3}$$

From preliminary voltage-current tests on the overlay panel, (ρ) for the conductive concrete is estimated at 156 ohm-in. The distance between electrodes, *l*, is a function of the number of electrodes used within each overlay panel. During a 5-year period, which included 14 winter storms, deicing at the Roca Spur Bridge in Nebraska required an average 32.5 W/ft^2 per winter storm. The average snow depth for these storms was 6.1 in. with a 3.3- to 10.1-in. range [3]. Using a two-subsection configuration, as shown in figure 26, supplying 36V generates 10.8 W/ft^2 power density with a corresponding 6.0-amp current, figure 16. Considering a 36-hour inclement weather condition, the required amp-hours for the battery storage bank is 216 amp-hours (36 hr x 6.0 amp) and, therefore, deep-cycle batteries are warranted.

Thirty-six, 200-W solar panels were purchased from Sun Electronics for the study's PV energy system. The PV system has the capability of generating 7.2 kW for the 20- by 20-ft conductive concrete test mat (18 W/ft^2). Eleven 12V deep-cycle batteries (rated 195 amp-hr) were configured to develop the energy storage bank. Two battery storage banks were configured using four 12V batteries wired in series to develop a 48V potential difference. The third battery storage set included three 12V batteries in series to provide a total of 36V.

Platform frames were constructed to support the solar panels used for the PV system, figure 35. The solar panels were fastened to the support and positioned in the test area facing south, figure 36. Thirty-two panels were included in the system to generate 6.4 kW of power. Four panels were set aside as backup for future work as needed.

Figure 35. Solar Panel Supports

Figure 36. Solar Panels Positioned Within the Test Area

6.3 THE PV ENERGY CONTROL.

The PV system is configured with a regulator built by the UA, figure 37, which controls the amount of energy delivered to the battery storage bank and to the overlay panels. Solar panels supply DC voltage to the battery storage banks to ensure that the batteries are fully charged.

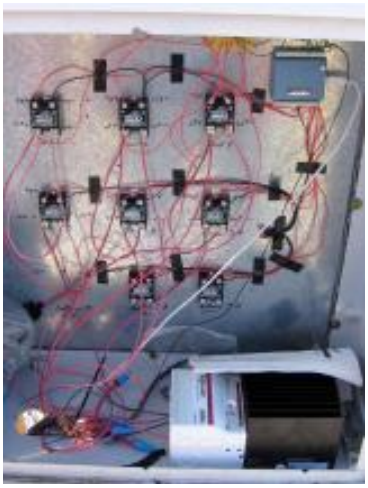

Figure 37. Regulator

Excess energy is routed to the overlay panels. The batteries provide a source for continuous energy to the overlay panels. Additional energy is provided to the overlay panels, when available, directly from the solar panels. The regulator was designed to allow the user the flexibility to set upper and lower limits to direct whether the battery storage bank or the overlay panels are being energized, figure 38. Consequently, energy is first routed to the batteries until they are topped at full voltage by setting the "Battery High Limit" value shown in figure 38. After the batteries are at the "Battery High Limit" voltage, the regulator routes energy directly to the overlay panels to raise pavement temperature. During evening hours and no-light time periods, the regulator routes energy from the batteries to the concrete overlay panels to help maintain the slab temperature.

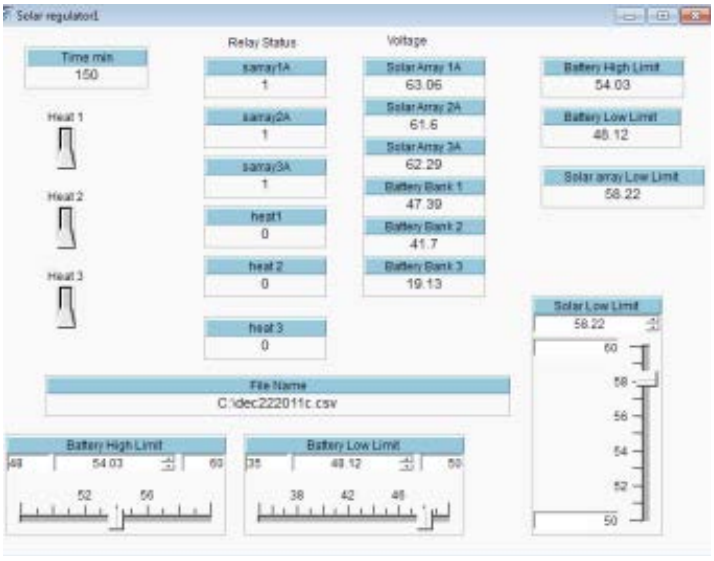

Figure 38. The PV Energy System Recorded Measurements

6.4 DATA RECORDING.

A data acquisition (DAQ) system, figure 39, continually recorded temperatures from near-surface thermocouples located within the overlay panels, figure 40. The recorded temperatures were placed into a text file, which could be converted to a Microsoft® Excel® spreadsheet file for data processing. The DAQ also recorded the PV system voltages in a similar manner. The recording system was configured to enable remote connection.

Figure 39. The DAQ System

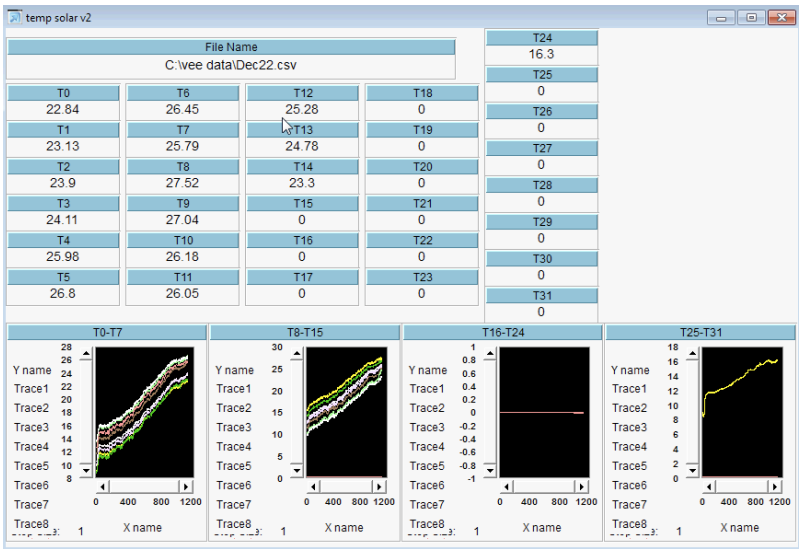

Figure 40. Temperature Measurements

7. OVERLAY HEAT TESTS.

7.1 TEST PROCEDURE.

Several heat tests were performed to determine heat uniformity, heat capacity, heating rate, and power consumption. Test mat temperature readings were taken at 1- by 1-ft, interior-grid panel points over a 4- by 10-ft overlay panel so that a total of 27 temperatures were monitored. Typically, heat tests for an overlay panel were conducted at night so that the sun would not influence temperature results. Each test began approximately at 12:30 a.m. and finished at 6:30 a.m. Temperature readings were taken for both the conductive concrete mat as well as the control mat, which was constructed of conventional concrete, at both start and end times. Temperatures were measured using thermocouples embedded in the concrete and also by using an infrared thermometer.

7.2 THERMOCOUPLES.

Type T (copper and copper/nickel alloy) thermocouples were used for temperature measurements. Thermocouples were placed in the control mat at 3-ft, 2-in. spacing along the control slab centerline, as shown in figure 18. The thermocouples were positioned at a 0.5-in. depth below the pavement surface. Conductive concrete Test Mat No. 1 included a total of nine thermocouples. Three thermocouples were spaced down the centerline of each electrode pair at a 3-ft, 2-in. space from the test mat ends. Additional thermocouples in the center of the slab were used in Test Mat No. 1 to measure temperatures at a 3.5-in. depth and at an 11-in. depth. Test Mat No. 2 had six thermocouples with three thermocouples spaced equally down the centerline of each electrode pair. Each thermocouple was at a 0.5-in. depth. Test Mat Nos. 3 through 10 had two thermocouples each located 5 ft along the panel length and at mid-length between the electrodes.

7.3 INFRARED THERMOMETER.

A PCE-IR 425 infrared thermometer was used to read surface overlay panel temperatures. The infrared thermometer has a temperature range of -60° to 1000°C with a reading accuracy of ±2°C. The infrared thermometer readings supplemented the thermocouple readings during heating tests.

7.4 ICE TEST.

To examine the suitability of the system during inclement weather conditions, an ice test was conducted on July 27, 2011. Four 12V deep-cell batteries in series (51.7V) were connected to electrodes 1 and 3 of the Test Overlay 1 conductive concrete overlay panel, figure 41. Stored battery energy was considered during this test to simulate energy availability during inclement weather conditions. Because of high daytime temperatures at the time of testing, the test was conducted in the evening. Initially, no energy was supplied to the overlay conductive concrete test mat, Time 0 (12:00.a.m.), figure 42. At 2:00.a.m., Time = 120 min on figure 42, energy was supplied to Test Overlay 1, and the thermocouples near the energy supply, T7 and T10, experienced a temperature increase, figure 42. Conversely, the thermocouple furthest from the

power supply, T4, experienced minimal temperature change. The ambient temperature remained fairly constant while the control mat made using conventional concrete experienced cooling.

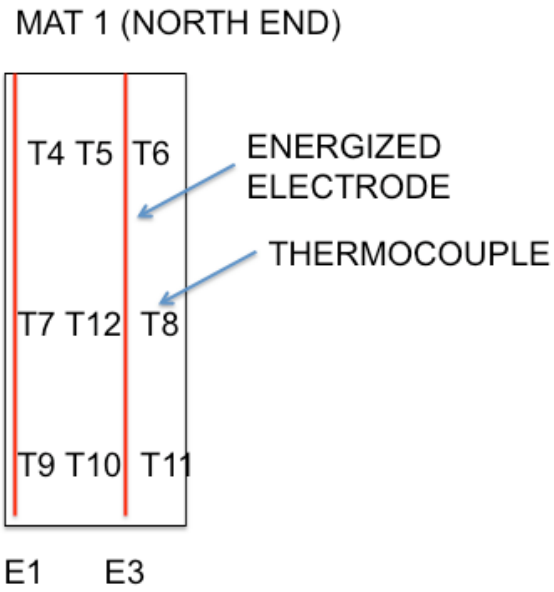

Figure 41. Thermocouple Locations on Overlay 1

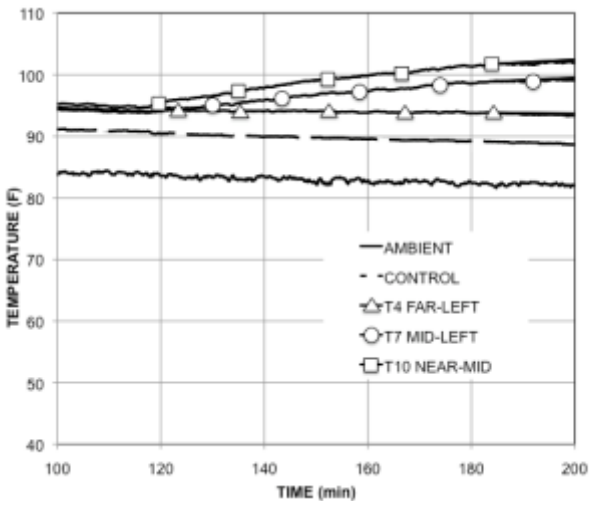

Figure 42. Ice Test—Overlay 1

At 7:30.a.m., a thin layer of ice was uniformly spread over the 4- by 10-ft conductive concrete overlay panel, Overlay 1, and on the 4- by 10-ft control panel, figure 43. The measured battery voltage at 7:30 a.m. was 46.5V. After the ice was applied, Time 0 on figure 44, the ambient temperature increased because of daylight. At Time 0, both the conductive concrete mat and the control mat experienced a significant surface temperature reduction due to the ice. However,

subsequent to the temperature reduction, the energized conductive concrete overlay rebounded much faster than the control mat, figures 43 and 44. (In each figure, the control test mat is shown on the left side, and the conductive concrete overlay is shown on the right.)

(a) Time 0 (ice application) (b) Time = 25 minutes

Figure 43. Ice Test at (a) Time 0 and (b) Time = 25 Minutes

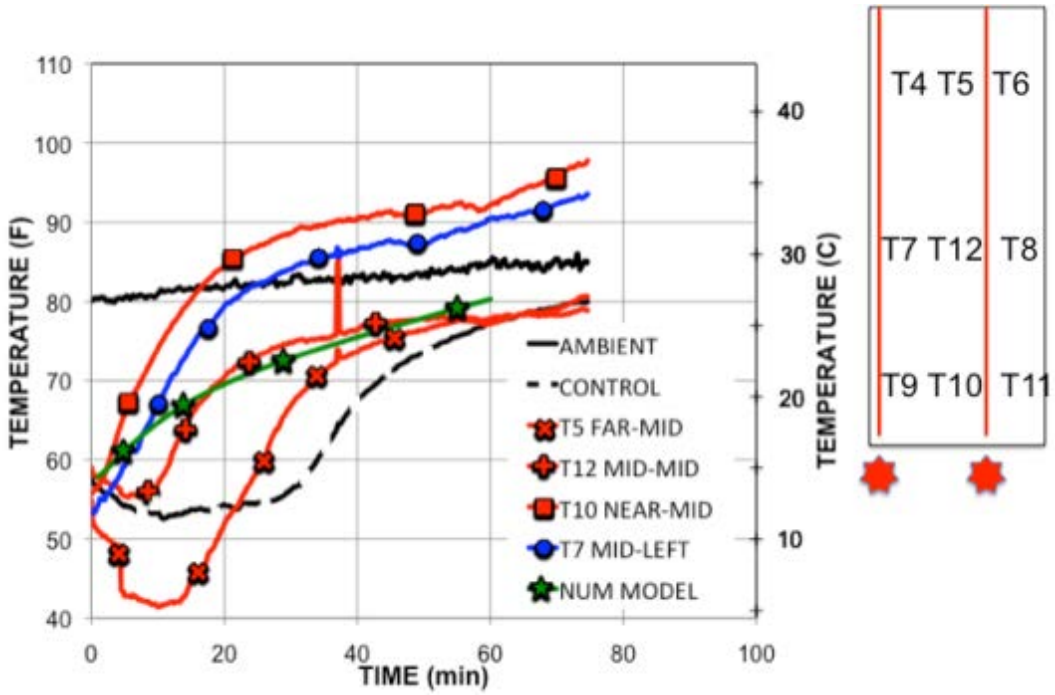

Figure 44. Overlay Panel Response to a Thin Ice Layer

7.5 EXPERIMENTAL TEST OVERLAY RESULTS.

7.5.1 Overlay 1.

To examine the potential benefits of pavement heating, the energized conductive concrete Overlay 1 and the control test mat were compared over a 5.5-hour period on July 29, 2011. Because of high daytime temperatures at the time of the test, the heat test was conducted in the

evening. Prior to the test, four 12V deep-cell batteries in series (approximately 48V) were fully charged using solar energy during daylight. At 12:30 a.m., energy from the battery bank was introduced to the conductive concrete of Overlay 1 by connecting jumper cables to electrodes 1 and 3 (E1 and E3) of the conductive concrete overlay panel, figure 45. Both cables were connected at the south end of the panel. The actual measured voltage supplied to the conductive concrete mat was 50.2V. Initial temperatures were recorded using an infrared thermometer at equally spaced, 1-ft grid points over the entire 4- by 10-ft conductive concrete panel, figure 45. At the start of the test, the control mat showed a slightly lower temperature, 88.3°F, than the conductive concrete test mat, and both the test mat and control mat showed higher temperatures than the ambient temperature. At 6:00 a.m., before sunrise and 5.5 hours after energy was initially introduced, temperature readings were again recorded, figure 45. At 6:00 a.m., ambient temperature decreased to 75.2°F and the control mat temperature decreased by 4.5°F. The results show non-uniform final temperature distribution with significant temperature increase at the test overlay's south end where the energy was supplied; however, insignificant changes in temperature at the north end.

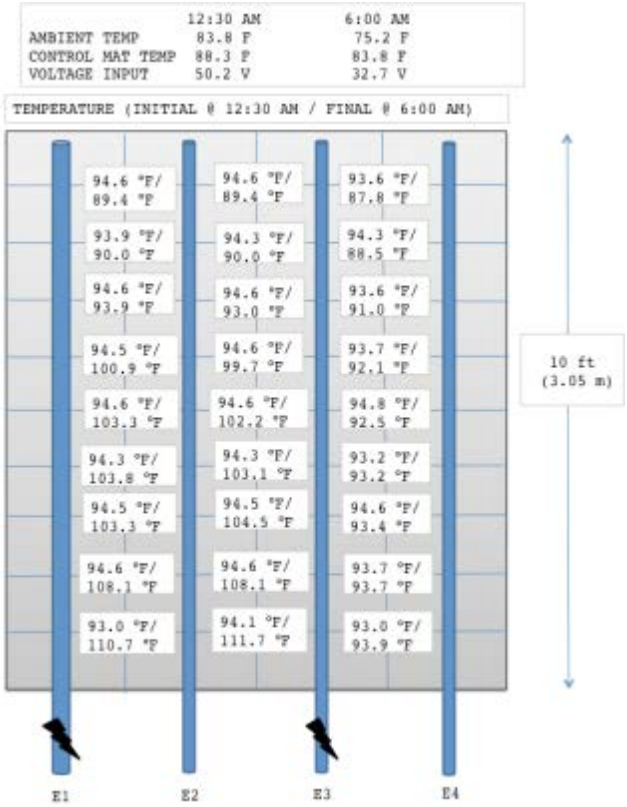

Figure 45. Surface Slab Temperatures at Overlay 1; July 29, 2011

Additional temperature measurements were recorded for the test mat to better understand the cause of the non-uniformity in the results. The location in which energy was introduced to Overlay 1 was modified in the next test so that battery jumper cables were connected to electrodes 1 and 3 (E1 and E3); however, the jumper cable at E1 was connected at the north end, figure 46. Similar to the first test, temperatures at the south end showed a significant temperature increase. The temperature change was insignificant at the north end; however,

temperature measurements showed a temperature gradient moving toward the south end. The region outside the E1-E3 energized area showed some temperature increase.

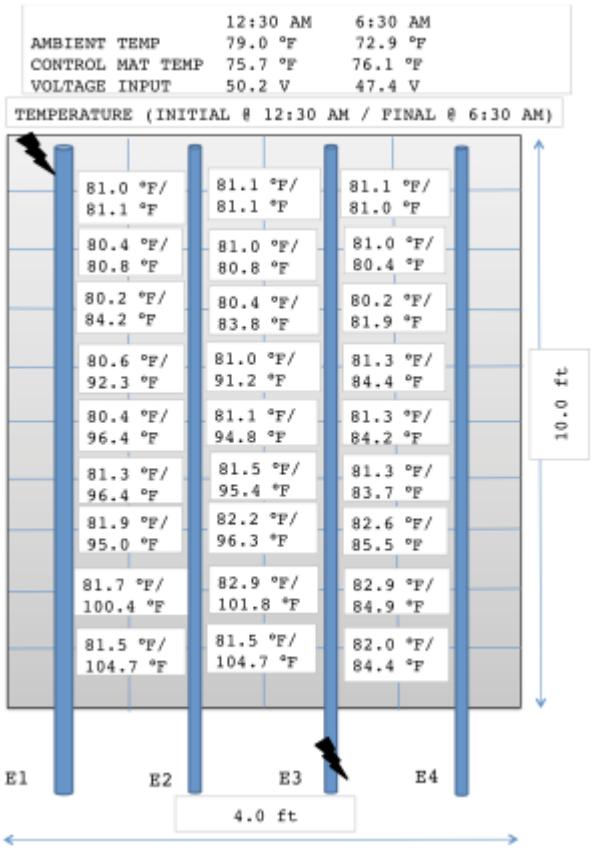

Figure 46. Surface Slab Temperatures at Overlay 1; August 9, 2011

A third test was conducted on Overlay 1 to investigate the significance of where energy was introduced to the overlay panel and temperature distribution. In the third test, battery jumper cables were attached to electrodes 1 and 3 (E1 and E3); however, both cables were connected to the electrodes at the north end, figure 47. Similar to the first two tests, temperatures at the south end showed a significant temperature increase, but little change was identified at the north end. The region outside the E1-E3 energized area showed some temperature increase.

From the three tests, it was concluded that the non-uniform temperature distribution could be attributed to the non-uniform steel fiber distribution in the overlay panel caused by placing the panel in three lifts.

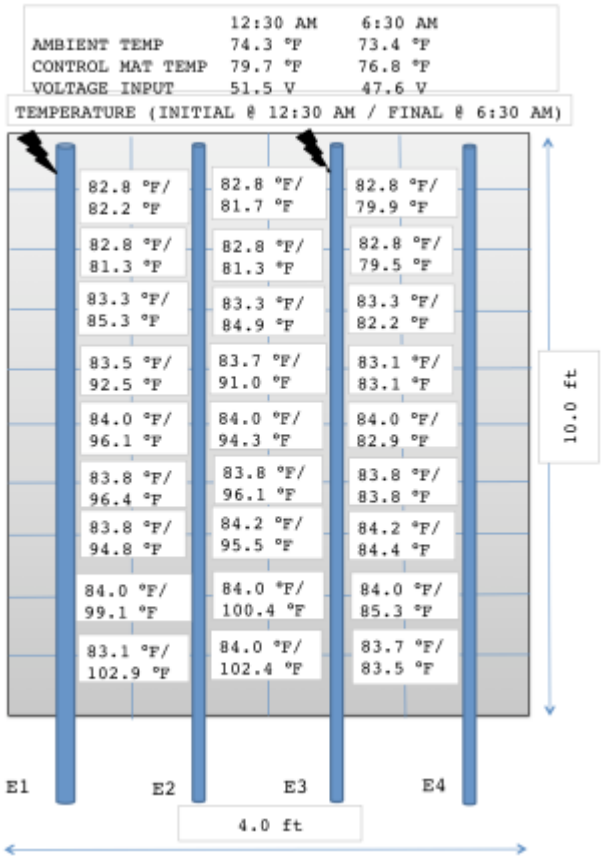

Figure 47. Surface Slab Temperatures at Overlay 1; August 16, 2011

7.5.2 Overlay 2.

Surface slab temperatures were recorded at Overlay 2 on September 2, 2011. Overlays 2 through 10 used an electrode layout that created two equal energy subregions, figure 48. Two sets of two batteries (2 x 12V = 24V) were used, in which one battery set was attached between E1 and E2 and the second set between E3 and E4. Consequently, energy was supplied to the entire overlay. Temperature decrease is identified throughout the overlay; however, final temperatures in Overlay 2 are greater than the control overlay final temperature. The temperature gain, which was less than anticipated, was later attributed to thermal shrinkage cracking that developed during the concrete curing process.

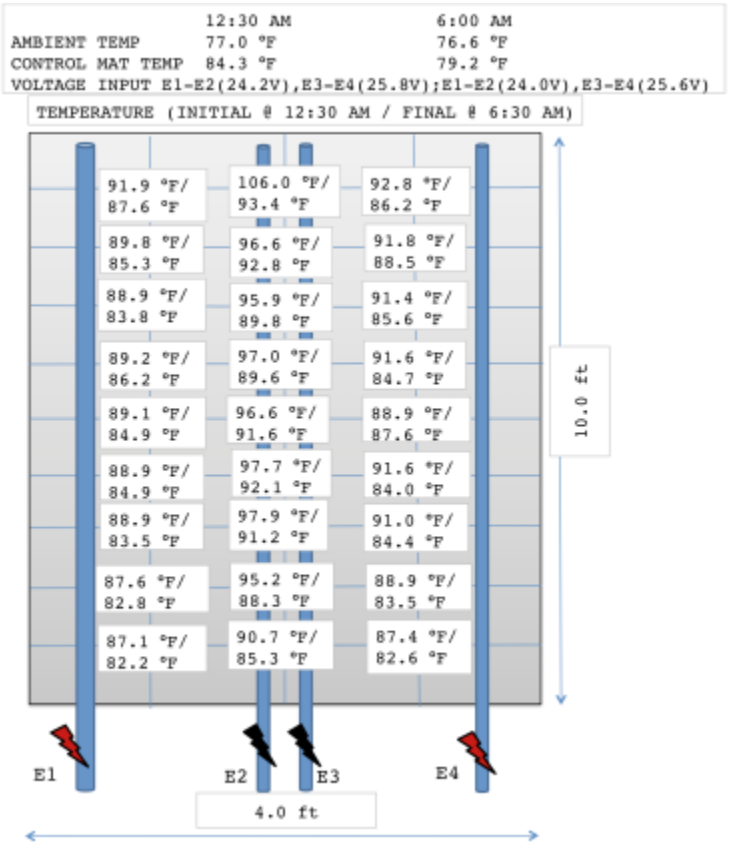

Figure 48. Surface Slab Temperatures at Overlay 2; September 2, 2011

7.5.3 Overlay 3.

Surface slab temperatures were recorded at Overlay 3 on October 6, 2011. Overlay 3 used a similar electrode layout to the one used in the Overlay 2 test, figure 49. Four batteries in series (4 x 12V = 48V) were used to energize a section of Overlay 3. Battery cables were connected to E3 and E4. Temperature increase is identified within the subregion between E3 and E4. Conversely, the subregion between E1 and E2 experienced no temperature increase. The Overlay 3 temperature recordings are more uniform than Overlay 1, suggesting a more homogeneous mix for this panel.

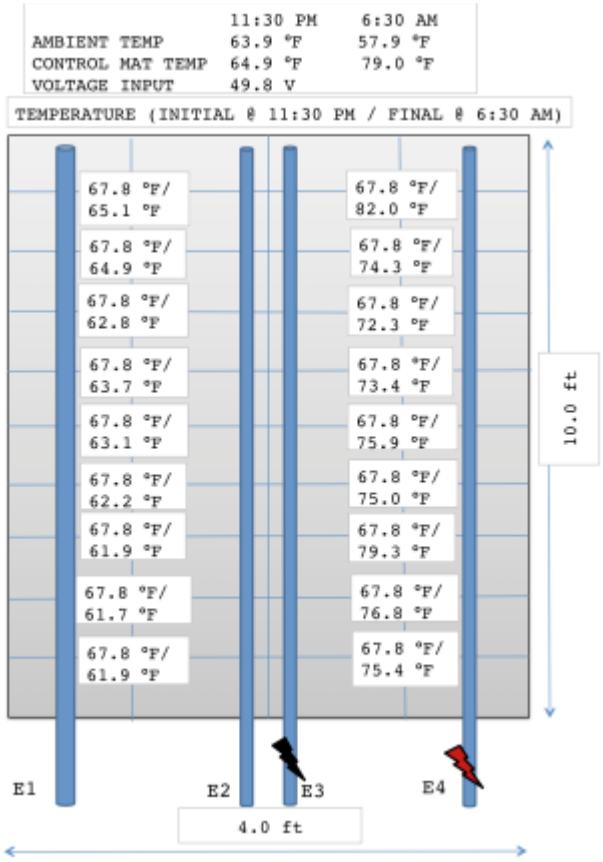

Figure 49. Surface Slab Temperatures at Overlay 3; October 7, 2011

Surface slab temperatures were recorded at Overlay 3 on November 29, 2011. Similar to the test performed on October 7, 2011, surface slab temperatures were measured over a 5- to 6-hour period to monitor the temperature change resulting from the application of 48 volts of direct current (VDC), figure 50. Converse to previous temperature tests, the ambient temperature was lower and was subfreezing. Four batteries in series were used to energize the section of Overlay 3 between E3 and E4. A slight temperature increase was identified within the subsection between E3 and E4; however, no energy impact was evident in the subsection between E1 and E2. The minor temperature change measurements correspond to a lower conductive concrete conductivity due to the low temperature. Conductive concrete's electrical conductivity is a function of temperature and increases as temperature increases.

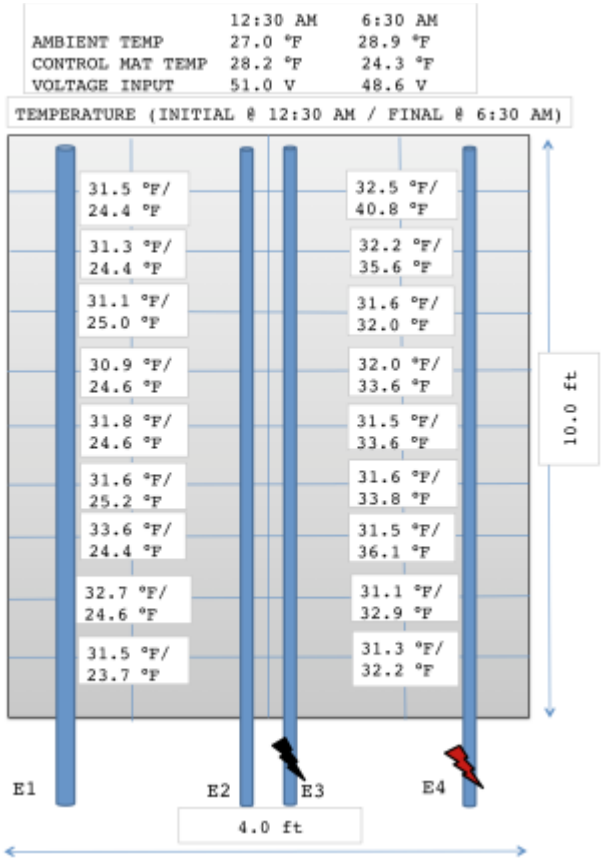

Figure 50. Surface Slab Temperatures at Overlay 3; November 29, 2011

7.5.4 Overlay 4.

Surface slab temperatures were recorded at Overlay 4 on October 20, 2011. Overlay 4 used a similar electrode layout to the one used in Overlays 2 and 3, figure 51. Four batteries in series (4 x 12V = 48V) were used to energize the section of Overlay 4 between E3 and E4 by connecting battery cables to E3 and E4. Over the study period, the ambient temperature decreased by 4°F, and the control mat temperature decreased by 5.6°F. Conversely, the temperature within the energized section of Overlay 4 remained constant. Final temperature distribution was fairly uniform, indicating a homogeneous mix for this overlay.

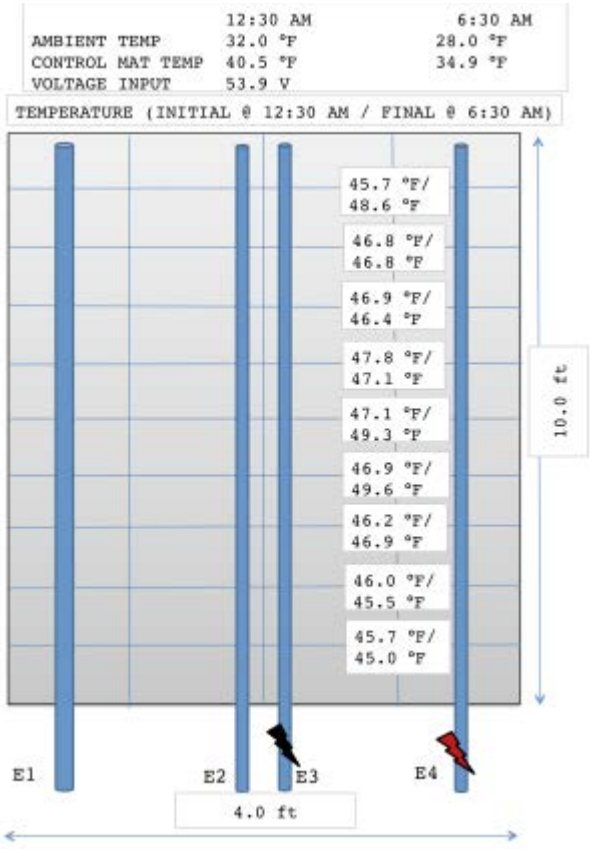

Figure 51. Surface Slab Temperatures at Overlay 4; October 20, 2011

7.5.5 Overlays 4 and 7.

Surface slab temperatures were recorded at Overlays 4 and 7 on November 28, 2011 after Overlay 7 was placed. Overlays 4 and 7 use a similar electrode layout to the one used in Overlay 2, figure 52. The 10-ft-long electrodes in Overlays 4 and 7 were connected using 1-in. threaded rod couplers. Four batteries in series (4 x 12V = 48V) were used to energize the sections of Overlays 4 and 7 between E3 and E4. Battery cables were connected at the south end of Overlay 4 to E3 and E4. Over the study period, the ambient temperature decreased by 2°F, while the control mat temperature decreased by 4.8°F. Conversely, the temperature within the energized sections of Overlays 4 and 7 showed a fairly uniform temperature increase. Additionally, the tests for these panels showed improved heat conductivity of the mix to the subregion outside of the energized near-field.

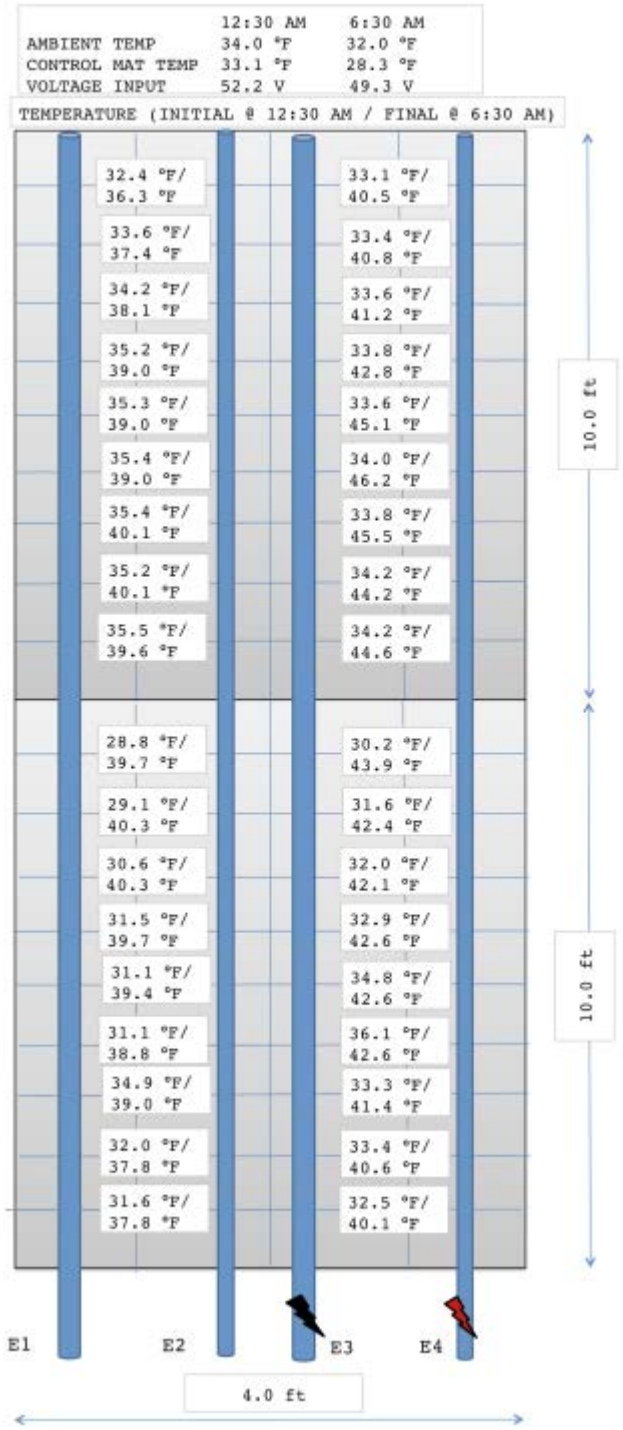

Figure 52. Surface Slab Temperatures at Overlays 4 and 7; November 28, 2011

7.5.6 Overlay Panel Heat Test Summary.

The initial and post-experiment recordings for the overlay tests are summarized in table 6.

Table 6. Overlay Heat Test Results Summary

Date (2011)	Overlay Number	Ambient Temperature (°F)	Voltage (VDC)	Average Overlay Temperature (°F)	Average Control Temperature (°F)
July 29	1	83.8/75.2	50.2/32.7	94.4/100.3	88.3/83.8
August 9	1	79.0/72.9	50.2/47.4	81.1/92.3	75.7/76.1
August 16	1	74.3/73.4	51.5/47.6	83.5/92.1	79.7/76.8
September 2	2	77.0/76.6	25.0/24.8	92.2/86.8	84.3/79.2
October 7	3	63.9/57.9	49.8/48.8	67.8/76.1	64.9/79.0
October 20	4	32.0/28.0	53.9/-	46.6/47.2	40.5/34.9
November 28	4 and 7	34.0/32.0	52.2/49.3	33.4/42.7	33.1/28.3
November 29	3	27.0/28.9	51.0/48.6	31.7/34.5	28.2/24.3

8. CONDUCTIVE CONCRETE NUMERICAL MODELING.

8.1 GOVERNING EQUATIONS.

Electric energy is supplied to a conductive concrete overlay through embedded electrodes within each overlay panel and converted to heat energy through Joule heating, which is heat generated from an electric current flowing through a conductor. Heat energy is distributed throughout the overlay panel through heat conduction. In the problem of heat flow through a conductive concrete mat, an electric field interacts with a thermal field. Consequently, the solution of temperature distribution within a conductive concrete overlay mat warrants a coupled-field analysis.

The governing equation for three-dimensional heat conduction is [17]:

$$\frac{\partial}{\partial x}\left(k\frac{\partial T}{\partial x}\right)+\frac{\partial}{\partial y}\left(k\frac{\partial T}{\partial y}\right)+\frac{\partial}{\partial z}\left(k\frac{\partial T}{\partial z}\right)+\frac{\partial Q}{\partial t}-\rho c_p\frac{\partial T}{\partial t}=0 \tag{4}$$

where $\frac{\partial Q}{\partial t}$ is the heat generation rate per unit volume, k is the thermal conductivity, ρ is mass density, c_p is the material-specific heat, and T is temperature. $\frac{\partial Q}{\partial t}$ and T are functions of coordinate position (x,y,z) and time (t). The thermal conductivity, k, is a function of position (x,y,z) and temperature (T); however, for the temperature range considered in this work, the thermal conductivity is taken as temperature independent. The governing equation for an electric field in a three-dimensional solid is [18]:

$$\frac{\partial}{\partial x}\left(\kappa\frac{\partial V}{\partial x}\right)+\frac{\partial}{\partial y}\left(\kappa\frac{\partial V}{\partial y}\right)+\frac{\partial}{\partial z}\left(\kappa\frac{\partial V}{\partial z}\right)=0 \tag{5}$$

where V is the electric potential and κ is the electrical conductivity. V is a function of coordinate position (x,y,z) and time (t). Electrical conductivity is a function of temperature (T). For the

temperature range considered in this project, electrical conductivity is a function of temperature. Heat is generated in the conductive concrete overlay panel as current moves from one embedded electrode within the overlay panel to another embedded electrode. Joule's First Law, which relates heat to current flowing through a conductor, describes the heat generated from the electric current within the overlay panel:

$$\kappa\left(\left(\frac{\partial V}{\partial x}\right)^2+\left(\frac{\partial V}{\partial y}\right)^2+\left(\frac{\partial V}{\partial z}\right)^2\right)-\frac{\partial Q}{\partial t}=0 \tag{6}$$

Equation 6 describes Joule heating, internal heat generation in a solid due to an electric potential. Equation 6 also identifies heat generation's dependency on the material's electrical conductivity. Equations 4 through 6 are coupled, and therefore, their solution warrants an iterative numerical approach [19].

8.2 BOUNDARY CONDITIONS.

Boundary conditions to solve the Joule heating problem are established from energy balance along the solid surface [17]. With no imposed external heat flux and neglecting radiation heat flux, energy balance at the surface requires:

$$+q_n = q_{cvB} \tag{7}$$

The heat flux normal to the boundary surface, q_n, is equal to the convection heat flux at the boundary, q_{cvB}. q_n is written in terms of temperature using Fourier's law of heat conduction:

$$q_n = -k\left(n_x\frac{\partial T}{\partial x}+n_y\frac{\partial T}{\partial y}+n_z\frac{\partial T}{\partial z}\right) \tag{8}$$

n_α represent surface normals and are considered positive acting outward from the solid. q_{cvB} is written in terms of temperature using Newton's law of cooling:

$$q_{cvB} = h_B(T - T_{aB}) \tag{9}$$

where h_B is the convective heat transfer coefficient, T is the temperature at the considered boundary point and T_{aB} is the ambient temperature at the boundary point. The boundary condition equation is derived by substituting equations 8 and 9 into equation 7:

$$-k\left(n_x\frac{\partial T}{\partial x}+n_y\frac{\partial T}{\partial y}+n_z\frac{\partial T}{\partial z}\right) = h_B(T - T_{aB}) \tag{10}$$

The solution for Joule heating uses a numerical solution process involving iterative calculation steps [19]. Electrical conductivity, κ, is a material property and a function of temperature. The solution process begins by assuming a temperature field, T. The electrical conductivity field, κ, in equation 6, is approximated from the assumed temperature field. An electric potential field, V, is determined from equation 5 and introduced into equation 6 to calculate the heat generation rate

per unit volume, $\frac{\partial Q}{\partial t}$. The temperature field, *T*, is calculated using equation 4. Finally, the initially assumed temperature field is compared with the calculated temperature field of equation 4 for convergence. Iterative calculation cycles continue until temperature field convergence between the assumed and calculated *T* is attained. A numerical algorithm for thermoelectricity is included in ANSYS, a commercially available finite element code.

8.3 FINITE DIFFERENCE NUMERICAL MODEL.

In the preliminary work of this study, a numerical model was calibrated to the test overlay results in order to develop a future analysis tool for the proposed system. The numerical code used for this preliminary work was formulated using the finite difference method and is based on the governing equation for heat conduction, equation 4. Only the approximate area within the energized electrodes was considered. For this example, energy was supplied to electrodes E1 and E3, figure 41. Consequently, only a 33-in. by 10-ft (0.84- by 3.05-m) section was discretized for the numerical analysis, figure 53. The 33-in. width was discretized using 51 points spaced at 0.66-in. intervals while the 10-ft length spaced 101 points at 1.2-in. intervals. In the vertical direction, z, both the conductive concrete overlay and the base mat used 15 points spaced at 1-in. intervals. Because the conductive concrete overlay was bordered by wood, insulated temperature boundary conditions were applied for heat transfer in the horizontal directions, x and y. In addition, an insulated boundary condition was introduced at the boundary between the soil and base mat. Boundary condition details are included in figure 53. A heat source in the plane of the electrodes was used to simulate the heat generated in the conductive concrete. To model the ice test discussed in section 7, after ice was applied to the overlay surface, the temperature at the top three grid points (i.e., surface and two grid points below) were assumed to show the effects of the applied ice and, therefore, to experience a significant temperature reduction to 57°F. Conversely, the grid points below the third grid point were assumed to be initially at 80°F, approximately the ambient temperature. Because of ice melting, heat loss at the overlay surface was non-uniform. A heat loss value for ice was calibrated using actual ice test results. The effect of ice at the top surface was considered by providing a heat loss in addition to natural air convection. Heat loss is assumed to linearly decrease to zero as a function of time. Future work will investigate improving the model for heat loss at the overlay surface.

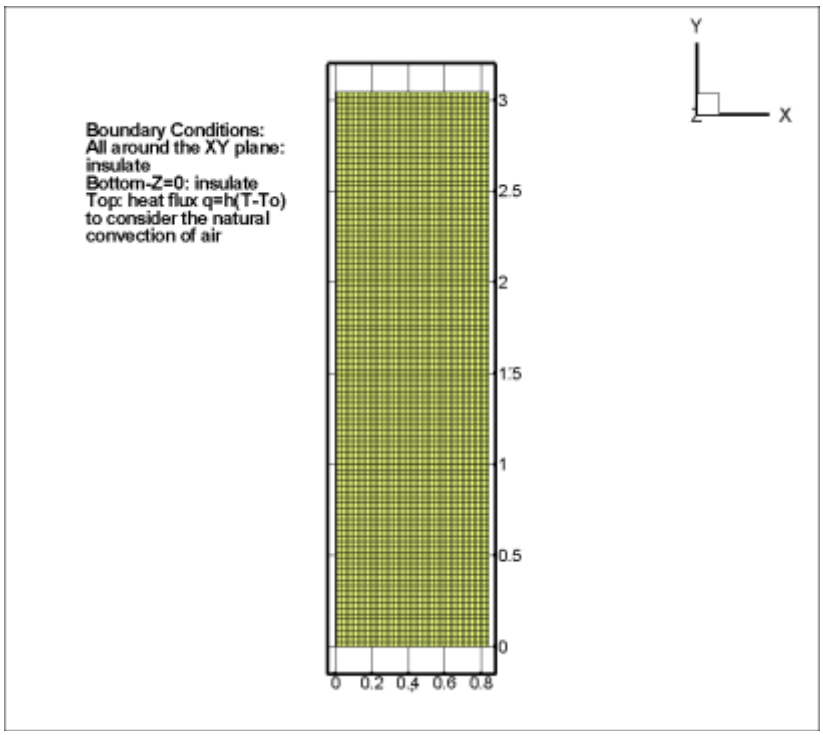

Figure 53. Grid XY Plane View With Boundary Conditions

Results using the finite difference numerical model are superimposed on figure 44 to show the predicted temperature increase trend of the conductive concrete mat. A cross-sectional view, looking at the 33-in. width (E1-E3) of the conductive concrete mat is shown in figure 54 with ice test temperature contours at 60 minutes. Heat primarily flows to the top surface to melt the ice. Conversely, minimal heat is dissipated at the bottom surface due to the insulated boundary condition at the bottom surface.

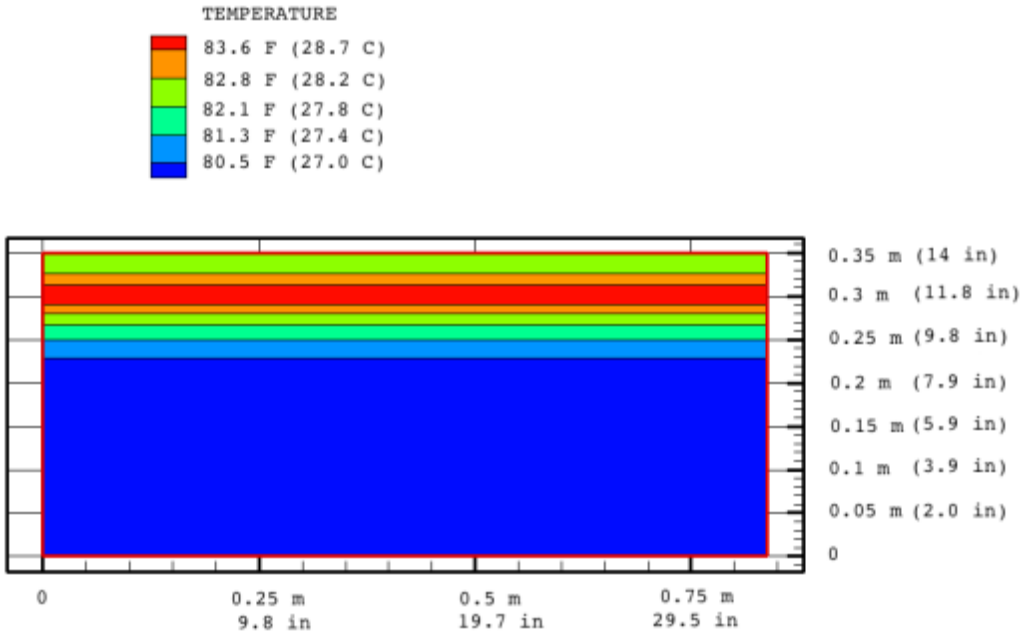

Figure 54. Predicted Temperature Distribution Using a Preliminary Numerical Model

9. CONDUCTIVE CONCRETE COST ANALYSIS.

Deicing costs using chemical treatment include deicing chemicals, equipment costs, labor, and maintenance costs incurred due to repair work of deteriorated pavements from deicing chemicals. Costs related to snow and ice removal are significant. At MSP in St. Paul, MN, approximately $4 million is budgeted for airside/runway snow removal.

Although the startup costs for a conductive concrete system powered by PV energy are high, the maintenance cost is minimal. Table 7 gives an outline of material costs for a conductive concrete overlay system.

Table 7. Cost Analysis

Material	Cost per Unit ($)	Amount of Material Needed per Unit	Total Cost per 4-in.-thick, 4- by 10-ft Overlay Panel ($)	Total Cost per ft^2 (4-in.-thick panel) ($)
Carbon powder (lb)	0.72	650 lb/yd^3	231.10	5.78
Steel fibers (lb)	0.40	50 lb/yd^3	9.88	0.25
Conventional-weight concrete (yd^3)	120.00	1 yd^3	59.25	1.48
Conductive concrete			300.23	7.51
Steel electrodes (ft)	5.00	48 ft/panel	240.00	6.00
PV panels (each)	400.00	2	800.00	20.00
Deep-cycle batteries (12V)	250.00	2	500.00	12.50
Total Cost =			1840.23	46.01
Each 4-in.-thick overlay panel (4 by 10 ft) = 13.33 ft^3 = 0.494 yd^3				

The total initial cost of a conductive concrete system is significant when compared to initial costs of laying conventional concrete. However, the primary advantage to a solar-powered conductive concrete system is in the low operating costs. If sufficient power is applied, ice and snow does not accumulate on the concrete surface in a conductive concrete system, and the costs associated with deicing chemicals, heavy equipment costs, and deteriorated concrete repair are removed. Additionally, the cost savings attributed to reduced flight arrival and departure delays is an added benefit.

10. TEMPERATURE DIFFERENTIAL DUE TO SURFACE COLORING.

Concrete pavement acts as a thermal mass. Concrete absorbs heat when subjected to a heat source (sun) and discharges heat when the ambient temperature is lower than the concrete mass temperature. Additionally, a dark-colored pavement absorbs more heat energy than a light-colored pavement. Experiments were conducted during this study to investigate the influence of a dark-pigment pavement surface.

The surface of the north control mat, shown in figure 18, was spray-painted black to investigate the significance of pavement surface coloring, figure 55. Temperature results of the north control mat were compared with the temperature results of the unpainted south control mat. Thermocouples were positioned at the center of each control mat at the same depths for each mat: 1/2 in. (T15 and T19), 1 in. (T16 and T20), 3 in. (T17 and T21), and 10 in. (T18 and T22). Thermocouples T15 through T18 were located in the north control mat (painted surface) while thermocouples T19 through T22 were located in the south control mat (unpainted surface).

Figure 55. Painted North Control Mat

The results over a 36-hour period are shown in figure 56 and are notable since the costs to paint the pavement surface are minimal. The painted mat absorbed more heat energy during the warmest part of the day than the unpainted mat; however, the painted mat also discharged more

heat energy during the evening. The temperature difference between the painted and unpainted mats was greatest at the time of day when the mats reached their peak temperature. Conversely, the temperature difference between the painted and unpainted mats was lowest at the time of day (early morning) when the mats experienced their minimum temperature. As expected, surface painting most impacts the pavement surface temperature and has a decreasing effect on the pavement temperature as the depth increased. Figure 56 shows that as the thermocouple depth increases, there is a greater time differential between the surface peak and the temperature peak for a given depth.

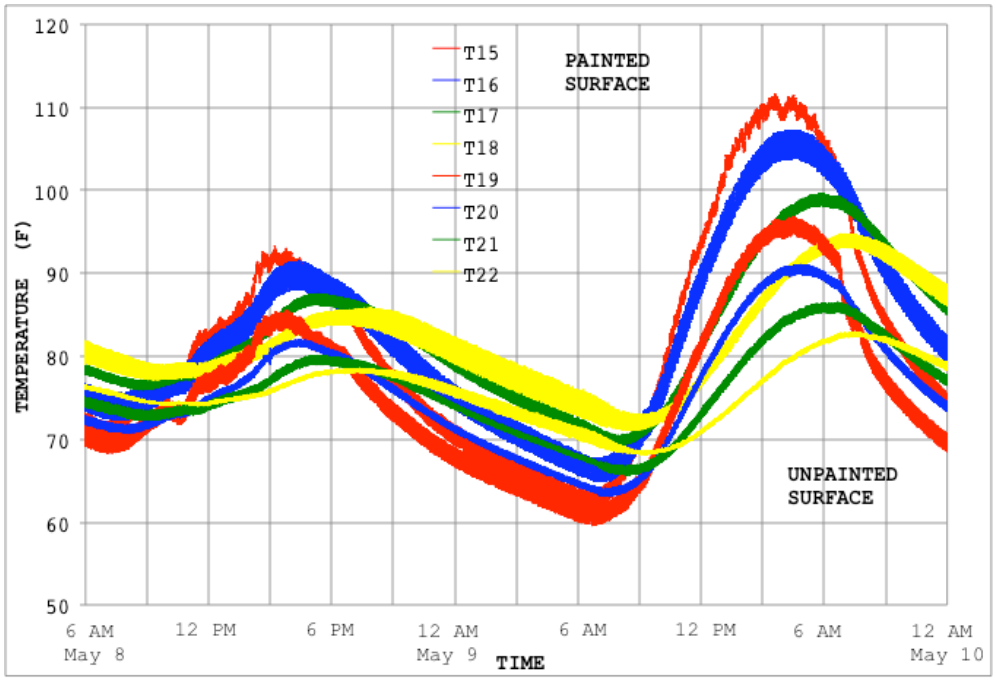

Figure 56. Temperature Recordings at Various Slab Embedment Depths

Figure 56 demonstrates the weaknesses of assuming the concrete mass to act as a thermal mass. The large temperature difference between the peak and valley of each temperature curve suggests that there is significant energy gain and loss through the pavement surface. Consequently, the premise of using the concrete pavement as a thermal mass in an anti-icing system needs to be revisited.

11. PRELIMINARY WORK USING SURFACE HEAT WIRES.

The greatest weakness in developing an anti-icing airfield runway system using renewable energy is the amount of energy warranted. The amount of energy necessary is prohibitive if the intent is to heat an entire 4-in.-thick overlay panel. Additionally, the amount of battery storage necessary to develop large amounts of energy is costly. With this in mind, the UA research team is investigating the concept of attaching copper wire heating elements to the pavement surface. Copper wire heating elements are found in car rear window defrosters.

A rear window defroster kit was purchased and attached to a 2- by 5-ft Lexan sheet, figure 57. The copper wires were spaced at 1.25 in. apart and in a serpentine configuration. Energy was applied to the heat wires through a bus bar. After attaching a 12V battery to the system, within 1.5 minutes, the wire temperature rose from 72.5° to 86°F with an accompanying 8.6 amps current. The results are promising and show the potential of using heat wires with a renewable energy system to develop an anti-icing system. Additionally, using heat wires is very economical. Challenges to this methodology include the proper attachment of the heat wires to the pavement surface and protecting the heat wires from damage by using an epoxy sealant.

Figure 57. Heat Wires

The copper wires were later attached to a concrete test mat to investigate the complications that may arise in attaching the wire configuration to concrete, figure 58. The concrete surface was smoothed and the wires attached to the concrete surface using the self-adhesive on the wires. Sikadur® 22, Lo-Mod epoxy was then applied to the wire surface as a sealant and for protection (see figure 58). A battery (12.4 VDC) was attached to the wire configuration shown in figure 58 and current flow was measured at 5.2 amps, which is equivalent to 64.5 W or a power density of 8.44 W/ft^2. The amperage is a function of the serpentine wire configuration and, therefore, can be easily changed through modifying the wire arrangement.

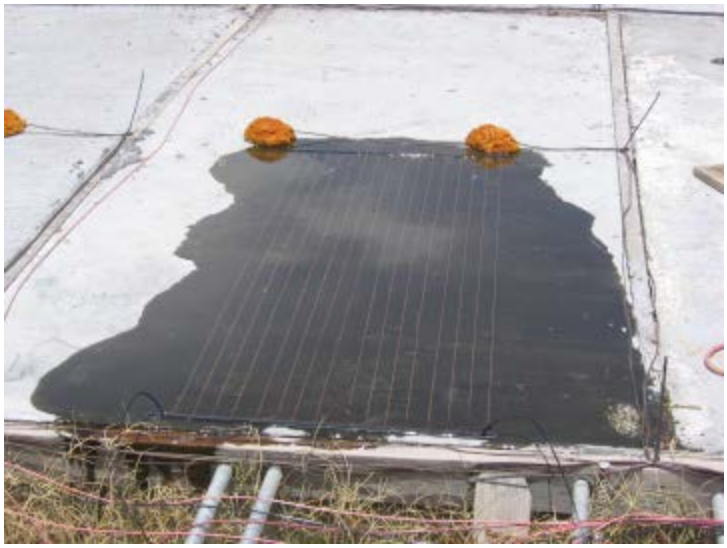

Figure 58. Heat Wires Attached to the Concrete Surface

12. CONCLUSIONS.

Snow, ice, and slush pavement conditions significantly impact aircraft operational safety. Snow removal typically involves plowing and chemical treatment. This process includes labor, heavy equipment, deicing chemicals, and labor, which can be costly to the airport operators who maintain runway surfaces. Additionally, inclement cold weather conditions significantly impact aircraft scheduling. This report presents an alternative approach for snow removal in which solar energy is coupled with conductive concrete to develop an anti-icing airfield pavement. If the runway slab surface can be maintained at an above-freezing temperature, snow and ice accumulation are prevented.

During this study, a 20- by 24-ft test mat was constructed at the University of Arkansas (UA) Engineering Research Center. The test mat consisted of twelve 4- by 10-ft overlay panels. Each overlay panel was 4 in. thick. A 10-in. base mat supported the overlay panels. Ten overlay panels were made using conductive concrete and two overlay panels were made using conventional concrete. The two control panels made of conventional concrete were used as a basis for the conductive concrete overlay panel results. A conductive concrete mix was formulated during this study and is presented in this report.

Each 4-in. by 4- by 10-ft overlay panel is a large thermal mass. However, the energy warranted to sustain this thermal mass at an above-freezing temperature is difficult to attain using a renewable energy system. Because of its large exposed surface area, an overlay panel is incapable of retaining sufficient thermal energy to melt snow. Therefore, larger amounts of energy than can be economically provided by the tested renewable energy system are warranted during sustained cold weather conditions.

Considering the weaknesses of heating a large mass with a large exposed surface and the limitations of a renewable energy system (i.e., energy storage), the UA research team also conducted preliminary experiments using heat wires, which can easily be combined with solar

energy to develop an anti-icing system. Early results showed potential; however, practical issues of installing and protecting heated wires under wheel loads need to be addressed before this approach can be viable.

13. REFERENCES.

1. National Aeronautics and Space Administration Langley Research Center, "Research Aims to Prevent Accidents on Hazardous Runways," FS-1999-07-45-LaRC, July 1999.

2. Ayres, M., Shirazi, H., Carvalho, R., Hall, J., Speir, R., Arambula, E., David, R., Wong, D., and Gadzinski, J., "Accident Database for ACRP 4-08 – Improved Models for Risk Assessment of Runway Safety Areas," Airport Cooperative Research Program Report 50, Transportation Research Board, Washington, DC, 2011.

3. Tuan, C.Y., "Implementation of Conductive Concrete for Deicing (Roca Bridge)," SPR-P1(04) P565, Final Report, Nebraska Department of Roads, July 2008.

4. Browning, J., Darwin, D., Gong, L., and Hughes, S.R., "Effects of Deicers on Concrete Deterioration," Structural Engineering and Materials Laboratory, University of Kansas, SL Report 07-3, December 2007, pp. 1-22.

5. Lee, H., Cody, R.D., Cody, A.M., and Spry, P.G., "Effects of Various Deicing Chemicals on Pavement Concrete Deterioration," *Mid-Continent Transportation Symposium 2000 Proceedings*, May 15-16, 2000, Iowa State University, Ames, Iowa, pp. 151-155.

6. Lund, J.W., "Reconstruction of a Pavement Geothermal Deicing System," *Geo-Heat Center Bulletin*, March 1999.

7. Tuan, C.Y., "Conductive Concrete for Bridge Deck Deicing and Anti-Icing," SPR-PL-1(037) P512, Final Report, Nebraska Department of Roads, July 2004.

8. Keranen, P., "Automated Bridge Deicers in Minnesota," *5th International Symposium on Snow and Ice Control Technology*, Roanoke, Virginia, 2000.

9. Roosevelt, D., "A Bridge Deck Anti-Icing System in Virginia: Lessons Learned From a Pilot Study," Final Report, VTRC 04-R26, Virginia Transportation Research Council, Charlottesville, Virginia, June 2004.

10. Wei, H. and Hongjun, Y., "Recovery Energy from the Separated and Gravity Type of Heat Pipe Exchanger in China," *Journal of Petroleum and Gas Engineering*, Vol. 2, No. 1, January 1-6, 2011.

11. Binghamton University, Staff, "FAA to Fund Students' Airport Pavement Project," *Inside Binghamton University*, September 2010.

12. Tuan, C.Y., "Roca Spur Bridge: The Implementation of an Innovative Deicing Technology," *ASCE Journal of Cold Region Engineering*, Vol. 22, No. 1, March 2008.

13. Whittington, H.W., McCarter, J., and Forde, M.C., "The Conduction of Electricity Through Concrete," *Magazine of Concrete Research*, Vol. 33, No. 114, March 1981, pp. 48-60.

14. Yehia, S., Tuan, C.Y., Ferdon, D., and Chen, B., "Conductive Concrete Overlay for Bridge Deck Deicing: Mixture Proportioning, Optimization, and Properties," *American Concrete Institute Materials Journal*, March-April 2000, Vol. 97, No 2.

15. ASTM International, ASTM A820 "Standard Specification for Steel Fibers in Fiber Reinforced Concrete."

16. Mooney, J.M., *Just Add Sunshine: Solar Electricity Will Set You Free*, ARC Press of Cane Hill, Cane Hill, Arkansas, 1997, pp. 1-105.

17. Stasa, F.L., *Applied Finite Element Analysis for Engineers*, CBS College Publishing, New York, New York, 1985.

18. Corson, D.R. and Lorrain, P., *Introduction to Electromagnetic Fields and Waves*, W.H. Freeman and Company, San Francisco, California, 1962.

19. Langerman, M.A., "Modeling the Steady-State ISV Process: A 3-D Finite Element Analysis of Coupled Thermal-Electric Fields," EGG-WM-9052, U.S. Department of Energy, 1990.